DOI 10.1515/aot-2013-0054 — Adv. Opt. Techn. 2013; 2(5-6): 369–395

Tutorial

Mikhail A. Vorontsov*

Speckle effects in target-in-the-loop laser beam projection systems

Abstract: In target-in-the-loop laser beam projection scenarios typical of remote sensing, directed energy, and adaptive optics applications, a transmitted laser beam propagates through an optically inhomogeneous medium toward a target, scatters off the target's rough surface, and returns back to the transceiver plane. Coherent beam scattering off the randomly rough surface results in strong speckle modulation in the transceiver plane. This speckle modulation has been a long-standing challenge that limits performance of remote sensing, active imaging, and adaptive optics techniques. Using physics-based models of laser beam scattering off a randomly rough surface, we show that received speckle-field spatial and temporal characteristics can be used to evaluate the intensity distribution of the beam projected onto the target. We derive analytical expressions that directly couple the measured target-return wave statistical characteristics, or 'speckle metrics', with characteristics of the laser beam intensity distribution on the target surface. We also show how measured speckle metrics can be utilized for evaluation of laser beam quality at the target surface and for adaptive compensation of atmospheric turbulence-induced phase aberrations.

Keywords: adaptive optics; atmospheric propagation; light scattering; remote sensing; speckles.

OCIS Codes: 030.6140, 010.0280, 010.1080, 010.1300, 010.1310.

***Corresponding author: Mikhail A. Vorontsov,** Intelligent Optics Laboratory, School of Engineering, University of Dayton, 300 College Park, Dayton, OH 45469, USA, e-mail: mvorontsov1@udayton.edu; and Optonicus, LLC East, Monument Ave Suite 101, Dayton OH 45402, USA, www.optonicus.com

1 Basic considerations for analysis

1.1 Target-in-the-loop and double-pass wave propagation configurations

There are a number of optical systems based on the so-called *target-in-the-loop* (TIL) wave propagation configuration. Figure 1A presents an example of this type of propagation geometry. In the TIL system types, a transmitted (outgoing) wave A propagates in an optically inhomogeneous medium along the optical axis (z-direction) toward a target, and after scattering off the target's surface at the plane $z=L$, the return wave ψ propagates back to the receiver plane $z=0$.

The optical system in Figure 1B offers a different example of the TIL propagation scenario where the target (scatterer) is the eye retina surface, and the optical inhomogeneities (eye lens aberrations) are located in the optical system pupil plane [1, 2]. The laser beam is focused onto the retina, and the scattered wave then propagates back through the same phase aberrations.

In contrast with 'unidirectional' (single-pass) wave propagation, optical waves in TIL systems propagate through refractive index inhomogeneities in both the forward (*outgoing wave*) and backward (*scattered* or *return wave*) directions. If the transmitter and receiver apertures are closely located or co-located, propagation of both waves may occur through practically the same refractive index irregularities. This results in a cascade of interesting effects known as *backscatter enhancement* [3–9].

The TIL propagation scenario with co-located transmitter and receiver apertures (*transceiver aperture*) is referred to as the *double-pass wave propagation* configuration, while the term target-in-the-loop is used to describe the more general case, including system configurations with spatially separated receiver and transmitter apertures.

The TIL wave propagation configuration is commonly encountered in a number of applications including military (laser target designation, active imaging, directed

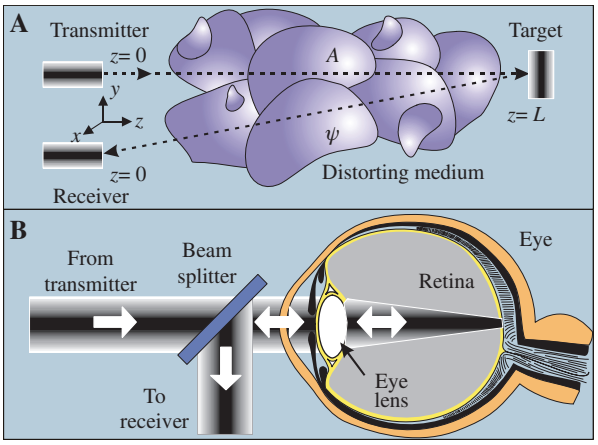

Figure 1 Target-in-the-loop wave propagation configurations with (A) wave propagation through a continuously distributed ('thick') optically inhomogeneous medium, and (B) through a medium with a 'thin' pupil-plane phase-distorting layer (eye-lens).

energy systems), laser technology (laser cutting, drilling, materials joining, additive laser manufacturing), laser medicine (laser tissue ablation, retina imaging, laser surgery), and remote sensing (remote spectroscopy, laser target tracking, laser vibrometry).

The performance of TIL systems depends on various factors: the transmitted laser beam wavelength, coherence, intensity and phase profiles, properties of the propagation medium's refractive index inhomogeneities, characteristics of the target (velocity, shape, surface roughness, reflection/scattering coefficient, etc.).

In many TIL applications, the target size may exceed the characteristic size of the illuminated area on its surface, referred to as the *target hit spot*. This corresponds to TIL system operation with *extended* and *noncooperative targets* [10–12]. In this case, characteristics of the return wave depend on the spatial distribution of the optical field on the target surface, as well as on the characteristics of the target itself. TIL propagation with laser beam scattering off an extended target represents one of the most challenging problem for remote sensing and wavefront control applications considered [13–15].

1.2 Spatial scales

Rigorous performance analysis of TIL systems is a complicated problem because of its strong dependence on multiple spatial and temporal scales. In most TIL propagation scenarios, the smallest spatial scales are related with the outgoing wave scattering off the rough target surface. Typical light scattering geometry is illustrated in Figure 2A, where rough surface at a point $\bar{\mathbf{r}}$ is described by the random profile function $z=\xi(\mathbf{r})$. Here, $\bar{\mathbf{r}}=\{\mathbf{r},z\}=\{x,y,z\}$ is the coordinate vector at a surface point. The correlation length l_s and rms σ_s of this function define the smallest characteristic spatial scales upon which the TIL propagation characteristics depend. In typical scenarios, l_s and σ_s are on the order of one to several hundred microns.

The largest spatial scale of TIL propagation is related with the characteristic size D_ψ of the return wave footprint at the receiver plane. The spatial scale D_ψ can be roughly estimated as $D_\psi \simeq L\theta_s$, where L is the distance to the target and $\theta_s \simeq \sigma_s/l_s$ is the characteristic angle of the surface roughness slope. Even for relatively smooth (mirror-like) surfaces, the footprint size can significantly exceed the receiver aperture diameter D. For very rough surfaces (large θ_s), the return wave footprint can be on the order of L – from hundreds of meters to tens of kilometers for typical TIL applications.

1.3 Computational issues

The ratio of the largest to the smallest spatial scales in TIL propagation scenarios can be enormous: $D_\psi/l_s \simeq 10^7$–10^{10}.

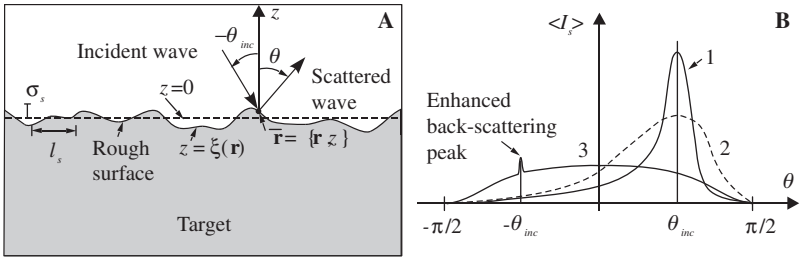

Figure 2 Wave scattering off a randomly rough surface: (A) scattering geometry; (B) notional representation of the scattered light intensity angular dependence (ensemble averaged over many roughness realizations) on the observation (scattering) angle θ for (1) mirror-like surface; (2) slightly rough surface; and (3) very rough surface. The narrow peak in the retroreflection scattering direction θ-θ_{inc} in curve (3) corresponds to the enhanced backscattering effect. In (A) a locally plane outgoing wave enters the surface at the incidence angle -θ_{inc}. Plane z=0 corresponds to the target surface in the absence of roughness.

This represents a serious problem for predictive numerical analysis of TIL systems.

The rule of thumb for such analysis states that the following considerations should be accounted for. First, the numerical grid pixel size l_{pix} (measured in units of physical length) should be smaller than the smallest spatial scale, that is $l_{pix}<l_s$. Second, the entire computational grid length $N_{pix}\cdot l_{pix}$ should be larger than the largest spatial scale D_ψ, where N_{pix} is the numerical grid size in pixels. The numerical grid size N_{pix} required for accurate numerical analysis of return wave propagation can be estimated by the ratio $N_{pix}\simeq D_\psi/l_s$. This order-of-magnitude estimation leads to the required numerical grid size $N_{pix}\simeq 10^7$–10^{10}, which significantly exceeds current computational capabilities.

There are some commonly used computational 'tricks' that allow to cope with this problem. Instead of D_ψ, the transmitter aperture diameter D is commonly utilized as the largest spatial scale, which leads to a more realizable number for the required grid size $N_{pix}\simeq D/l_s$.

In most cases, even this reduced grid size is still too large. Typically, D is on the order of tens to hundreds of centimeters and, correspondingly, $D/l_s\simeq 10^3$–10^5. A further decrease in N_{pix} up to a computationally affordable grid size of N_{pix}=512–1024 can be obtained via approximation of surface roughness by a random function having an artificially large correlation length ($l_s\simeq$1 mm or even larger). In addition, the surface roughness is commonly considered to be a δ-correlated random function with respect to the numerical grid.

Even these artificially imposed replacements of the largest and smallest spatial scales are typically insufficient. The scattered field localization area expands rapidly as the propagation distance increases and reaches the computational grid boundary at relatively short distances from the target. This leads to violation of the third important rule for numerical analysis: the grid size should be large enough so that both the optical field amplitude and first-order spatial derivatives of the field are always negligibly small at the numerical grid boundary (zero-field boundary conditions). Violation of these grid boundary conditions commonly results in instability of the computational process.

To avoid this computational instability associated with rapid increase in the return field localization area, the zero-field boundary conditions are imposed artificially. This is equivalent to considering TIL wave propagation inside a box of size $N_{pix}\cdot l_{pix}$ having absorbing walls. These artificially introduced absorbing walls result in auxiliary boundary diffraction that may impact computational accuracy. Although the absorbing walls allow stable numerical schemes, the obtained computational results can be inadequate.

1.4 Temporal scales

Additional obstacles for the analysis of TIL systems are the existence of multiple temporal scales: the time scale τ_{at} related with the dynamics of atmospheric turbulence effects, the characteristic time τ_{AO} of phase distortion compensation using adaptive optics (AO) technique, the time delay $\tau_d=2L/c$ related with double-pass wave propagation over the distance $2L$ at the speed of light c, and several other characteristic time scales τ_s associated with changes in the target surface roughness realizations inside the target hit spot.

For most atmospheric TIL beam control applications, the time scales obey the following inequality: $\tau_s<\tau_{AO}<\tau_d<\tau_{at}$. The slowest time scale is typically associated with the atmospheric parameter τ_{at}, which depends on the atmospheric turbulence conditions, wind speed, and beam slew. The time scale τ_{at} commonly varies from 10^{-1} to 10^{-3} s or even considerably less when tracking fast moving targets.

The fastest TIL temporal processes are related with changes in the target surface roughness pattern inside the illuminated area (target hit spot) of size b_s. For a target surface moving (or spinning) with linear velocity v_s, complete update of surface roughness realizations occurs at the time scale $\tau_s\simeq b_s/v_s$. Changes in surface roughness realization are dependent on several other factors including beam jitter, target surface vibration, and atmospheric turbulence-induced beam fluctuations and beam wander at the target surface. All of the factors associated with the scattering process may result in fast (on the order of tens of kHz or even higher) random fluctuations in the return field at the receiver plane.

For the case of target illumination using a broadband laser source, the time τ_s can be associated with the laser source coherence time $\tau_c\sim 1/\Delta\omega$, where $\Delta\omega$ is the laser frequency bandwidth. For broadband target illumination, the time scale τ_c can be negligibly small.

The difficulties in rigorous analysis of TIL propagation mentioned above highlight the importance of simplified models and analytical approximations that can be applied to the analysis of scattering and return wave propagation. In the following sections, we consider several such models.

2 Scattering and speckle-field propagation in a vacuum

2.1 Statistical models of randomly rough surfaces

A qualitative picture of optical wave scattering for targets with different surface roughness types is shown in Figure 2B. A slightly rough surface results in an attenuation of the specularly reflected outgoing beam intensity and the appearance of a diffuse component with a wide angular distribution for the scattered light intensity (curves 1 and 2 in Figure 2B). As the surface becomes more rough, the diffuse component increases, and the specular component practically vanishes (curve 3).

Analytical models that describe wave scattering depend on surface roughness characteristics such as the surface roughness height σ_s, correlation length l_s, surface roughness slope (the ratio σ_s/l_s), and the statistical model for the roughness profile function. The following two models are the most commonly used: small-amplitude perturbation [16–19] and the Kirchhoff (small-slope) approximation [17, 20, 21].

The *small-amplitude perturbative technique* is typically applied to slightly rough surfaces where the roughness amplitude rms σ_s is significantly less than the wavelength λ, and the roughness slopes are small $\sigma_s/l_s \ll 1$ (mirror-like surface).

The *small-slope approximation* is used for analysis of scattering from smooth surfaces with large roughness amplitudes where $l_s > \sigma_s \gg \lambda$. The condition $l_s > \sigma_s$ simplifies analysis because multiple-scattering effects can be neglected [17].

In the small-slope approximation, wave scattering at each point $\bar{\mathbf{r}}=\{\mathbf{r}, z(\mathbf{r})\}$ on the randomly rough surface is described in the geometrical optics approximation. At each point $\bar{\mathbf{r}}$, the optical field is represented as a sum of the incident wave and the wave reflected from the plane tangent to this point, as shown in Figure 3A. Contributions to the optical field scattered in the angular direction $\boldsymbol{\theta}$ originate from rough surface points, all of which have the identical tangent plane angular orientation. This means that all scattered field components in the direction $\boldsymbol{\theta}$ have the same polarization.

For closely located transmitter and receiver apertures, often referred to as the *small-angle scattering* condition, the scattered wave has the same polarization as the outgoing wave. Thus, with the small-slope approximation and under small-angle scattering conditions, depolarization effects can be neglected, and TIL propagation can be described using scalar fields having the same polarization for both the outgoing and scattered waves. Note that scattering off random surfaces with small-scale roughness, as well as multiple scattering (scattering off very rough surfaces), can result in a random depolarization of the scattered field [17].

The surface roughness profile function $\xi(\mathbf{r})$ is commonly described by a zero-mean, strictly stationary, isotropic, Gaussian random process. In this case, the two-point moment $\langle \xi(\mathbf{r}_1)\xi(\mathbf{r}_2)\rangle$ can be represented in the form [17, 20, 22]

$$\langle \xi(\mathbf{r}_1)\xi(\mathbf{r}_2)\rangle = \sigma_s^2 K_s(r), \tag{2.1}$$

where $\langle\ \rangle$ denotes ensemble-averaging over realizations of the random surface roughness, $\mathbf{r}_1$ and $\mathbf{r}_2$ are vectors in the target plane $r=|\mathbf{r}_1-\mathbf{r}_2|$, and $K_s(r)$ is the surface roughness autocorrelation function.

For most cases, a good approximation of the autocorrelation function is given by the Gaussian expression (*Gaussian surface*)

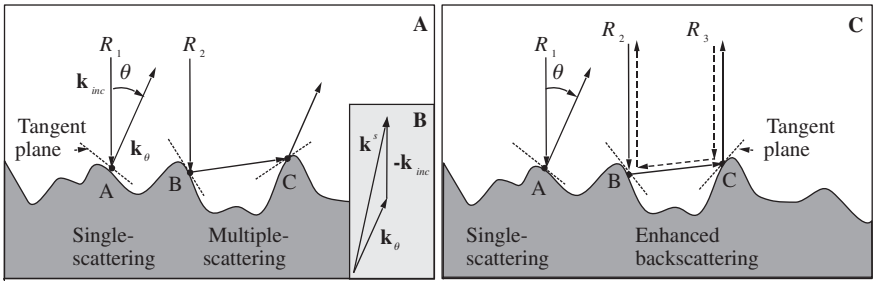

Figure 3 Geometrical representation of wave scattering for the case of an outgoing wave normally incident to the rough surface. For the single and multiple scattering shown in (A), optical rays are reflected from the corresponding tangent planes: ray trajectory R_1 corresponds to single scattering and ray trajectory R_2 to multiple scattering. Inset (B) illustrates the scattering process in terms of the scattering wavevector $\mathbf{k}^s=\mathbf{k}_\theta-\mathbf{k}_{inc}$, where $\mathbf{k}_{inc}$ and $\mathbf{k}_\theta$ are vectors orthogonal to the wavefronts of the incident and scattered waves, correspondingly. The ray trajectories R_2 (solid line) and R_3 (dashed line) in (C) are reciprocal. The scattering process associated with coherent summation of reciprocal waves results in the enhanced backscattering effect [22].

$$K_s(r)=\exp(-r^2/2l_s^2), \tag{2.2}$$

where l_s is the transversal roughness correlation length previously introduced.

2.2 Multiple-scattering and enhanced backscattering

Large surface roughness amplitudes and slopes (very rough surfaces) result in multiple scattering of the reflected light. Multiple-scattering geometry with the consequent specular reflection of light from two tangent planes (second-order scattering) is illustrated in Figure 3C. Compare single-scattering corresponding to the trajectory for ray R_1 with second-order scattering shown by ray R_2.

The graphical representation of multiple scattering in Figure 3C corresponds to the Kirchhoff approximation extended to analysis of the multiple-scattering phenomena [23]. Multiple scattering is responsible for the phenomenon known as the *enhanced backscattering effect* – the appearance of a well-defined peak in the angular dependence of the scattered field intensity in the retroreflection direction, as shown in Figure 2B [22, 24, 25].

The origin of this peak is associated with coherent interference between the double-scattered reciprocal waves, as illustrated in Figure 3C. The reciprocal ray trajectories R_2 and R_3 hit the surface at the same points, but in backward order. These reciprocal waves propagate the same distance and are always in phase. This leads to constructive interference between the reciprocal wavefronts and a factor of 2 increase (in theory) in the scattered wave's intensity in the retroreflection direction.

In practice, the measured enhanced backscattering (peak height in the retroreflection direction) is noticeably smaller than a twofold increase because of the dominant contributions from single scattering. For this reason, the enhanced backscattering peak can only be observed by averaging the speckle patterns that originate from wave scattering over many surface roughness realizations. The angular width of the enhanced backscattering peak is on the order of $\Delta\theta_{bs}\simeq\lambda/l_s$ for normal incidence to the target surface [22].

In TIL applications, wave scattering typically occurs off metallic (perfectly conducting) surfaces having large-scale surface roughness amplitudes ($\sigma_s\gg\lambda$) that are in many cases not necessarily smooth. Nevertheless, because of the dominant contribution from single-scattering processes, both the multiple-scattering and the enhanced backscattering contributions can typically be neglected (unless TIL system operation is based on these effects). For this reason, the small-slope approximation appears sufficient for analysis in most TIL wavefront control applications.

2.3 Scattered field boundary conditions

Consider for simplicity a rough surface oriented nearly orthogonal to the direction of outgoing wave propagation (z-direction), and assume that the small-slope approximation can be applied. Also assume that the complex amplitude of the incident wave at the target surface $A(\mathbf{r},\ z=L)\equiv A_T(\mathbf{r})=|A_T(\mathbf{r})|\exp[i\phi_T(\mathbf{r})]$ is a slowly varying function on the scale of the roughness correlation length l_s, where $|A_T(\mathbf{r})|$ and $\phi_T(\mathbf{r})$ are the modulus and phase, correspondingly. This means that the incident wave's wavevector $\mathbf{k}_{inc}(\mathbf{r})\equiv\nabla\phi_T(\mathbf{r})$ is a constant on the scale of l_s and that due to the outgoing wave's propagation in an optically inhomogeneous medium, variations in the vector $\mathbf{k}_{inc}(\mathbf{r})$'s direction occur over spatial scales significantly larger than l_s.

Define the scattering vector $\mathbf{k}^s(\mathbf{r})\equiv\{\mathbf{k}^s_\perp(\mathbf{r}),k^s_z(\mathbf{r})\}$ as $\mathbf{k}^s(\mathbf{r})\equiv\mathbf{k}_\theta-\mathbf{k}_{inc}(\mathbf{r})$, where $\mathbf{k}_\theta$ is a wavevector corresponding to scattering in the angular direction $\boldsymbol{\theta}$. For a target surface oriented nearly orthogonal to the outgoing wave's propagation direction and for relatively small scattering angles (small-angle scattering conditions), we have $|\mathbf{k}^s_\perp(\mathbf{r})|\simeq 0$ and, hence, $k^s_z(\mathbf{r})\simeq|\mathbf{k}^s(\mathbf{r})|$ (see Figure 3B).

It can be shown that under these assumptions the return wave complex amplitude at the target plane $\psi_T(\mathbf{r})\equiv\psi(\mathbf{r},\ z=L)$ can be approximated by the following boundary condition [17, 26]

$$\psi_T(\mathbf{r})=T(\mathbf{r})A_T(\mathbf{r})\equiv V(\mathbf{r})\exp[ik^s_z(\mathbf{r})\xi(\mathbf{r})]A_T(\mathbf{r}), \tag{2.3}$$

or equivalently,

$$\psi(\mathbf{r},z=L)=T(\mathbf{r})A(\mathbf{r},z=L)\equiv V(\mathbf{r})\exp[ik^s_z(\mathbf{r})\xi(\mathbf{r})]A(\mathbf{r},z=L), \tag{2.4}$$

where

$$T(\mathbf{r})=V(\mathbf{r})\exp[ik^s_z(\mathbf{r})\xi(\mathbf{r})]=\gamma(\mathbf{r})\exp[ikS(\mathbf{r})+ik^s_z(\mathbf{r})\xi(\mathbf{r})]. \tag{2.5}$$

The function $T(\mathbf{r})$ in expressions (2.3)–(2.5) describes the characteristic complex scattering coefficient for a target with a randomly rough surface, while the function $V(\mathbf{r})=\gamma(\mathbf{r})\exp[ikS(\mathbf{r})]$ corresponds to the scattering coefficient in the absence of roughness. Here, the phase function $S(\mathbf{r})$ depends on the target shape and orientation,

and the reflection coefficient $0 \le \gamma(\mathbf{r}) \le 1$ describes a target-induced complex field attenuation. In the case of an extended target with a flat surface, $\gamma(\mathbf{r})$ is a constant.

Formally, the scattering condition (2.3) coincides with the corresponding expression for a wave that, after reflection from a smooth (mirror-like) surface, passes through a thin random phase screen with the phase modulation function $\xi_s(\mathbf{r}) = k_z^s(\mathbf{r})\xi(\mathbf{r})$ [17, 26]. This phase modulation depends [through the scattering vector component $k_z^s(\mathbf{r})$] on the outgoing wave's wavefront slopes and, hence, on the wavefront phase aberrations at the target plane. (For most TIL systems, the outgoing wave's wavefront slopes at the target are much smaller than the surface roughness slopes $\theta_s = \sigma_s / l_s$; hence, $k_z^s(\mathbf{r}) \simeq k_z^s = \text{const.}$)

2.4 Speckle-field complex amplitude

In an optically homogeneous medium, scattered wave propagation from the target to receiver planes can be described in the parabolic (Fresnel) approximation of the diffraction theory by the following equation

$$-2ik\frac{\partial \psi}{\partial z} = \nabla_\perp^2 \psi \tag{2.6}$$

with the boundary condition (2.4). Propagation model (2.6) corresponds to the small-angle TIL propagation geometry with closely located transmitter and receiver apertures.

The solution of Eq. (2.6) at the receiver plane ($z=0$) can be represented in the form of the Fresnel diffraction integral as

$$\psi(\mathbf{r}, z=0) = c_0 \int\int_{-\infty}^{\infty} \tilde{\psi}_T(\mathbf{r}') \exp\left[-i\frac{k}{2L}\left|(\mathbf{r}-\mathbf{r}')\right|^2 + ik_z^s(\mathbf{r}')\xi(\mathbf{r}') \right] d^2\mathbf{r}', \tag{2.7}$$

where $c_0 = -ik/(2\pi L)$ is a constant, and

$$\tilde{\psi}_T(\mathbf{r}) = V(\mathbf{r}) A_T(\mathbf{r}) = \gamma(\mathbf{r}) e^{ikS(\mathbf{r})} A_T(\mathbf{r}) = \gamma(\mathbf{r}) e^{ikS(\mathbf{r})} A(\mathbf{r}, L) \tag{2.8}$$

is an auxiliary function that describes the scattered field complex amplitude at the target plane in the absence of roughness.

Propagation of the scattered wave to the receiver plane as described by the Fresnel integral (2.7) results in the formation of an optical field composed of randomly located bright and dark intensity spots. This field is commonly referred to as a *speckle field*. The spatial and temporal correlation properties of speckle fields play an important role in TIL wavefront control applications. Speckle-field statistical characteristics are discussed in the following subsections.

2.5 Mutual correlation function

Consider spatial correlation properties of the speckle-field complex amplitude. Define the mutual correlation function (MCF) of the speckle field at the plane z as the two-point product of the field complex amplitudes averaged over ensemble realizations of the random surface roughness

$$\Gamma_\psi(\mathbf{r}_1, \mathbf{r}_2, z) \equiv \langle \psi(\mathbf{r}_1, z) \psi^*(\mathbf{r}_2, z) \rangle, \tag{2.9}$$

where $\mathbf{r}_1$ and $\mathbf{r}_2$ are two vectors in the plane orthogonal to the direction of wave propagation. Note that for a return wave originating from an incoherent (e.g., star) or partially coherent monochromatic (quasimonochromatic) light source, expression (2.9) can also be referred to as the mutual intensity function or mutual coherence function [20, 27].

For the sake of convenience, we introduce the sum and difference coordinates

$$\mathbf{R} = (\mathbf{r}_1 + \mathbf{r}_2)/2, \quad \boldsymbol{\rho} = (\mathbf{r}_1 - \mathbf{r}_2). \tag{2.10}$$

With these coordinates the MCF can be represented as

$$\Gamma_\psi(\boldsymbol{\rho}, \mathbf{R}, z) \equiv \langle \psi(\mathbf{R} + \boldsymbol{\rho}/2, z) \psi^*(\mathbf{R} - \boldsymbol{\rho}/2, z) \rangle. \tag{2.11}$$

2.6 Propagation of the mutual correlation function

For return wave propagation in an optically homogeneous medium, the mutual correlation function at the receiver plane z=0 can be obtained by substituting the Fresnel diffraction integral (2.7) into Eq. (2.11). Omitting routine algebraic derivations we obtain

$$\Gamma_\psi(\boldsymbol{\rho}, \mathbf{R}, z=0) = |c_0|^2 \int\int \tilde{\psi}_T(\mathbf{R}' + \boldsymbol{\rho}'/2) \tilde{\psi}_T^*(\mathbf{R}' - \boldsymbol{\rho}'/2) F_\xi(\mathbf{R}', \boldsymbol{\rho}') \times \exp\left[i\frac{k}{L}(\boldsymbol{\rho}'\mathbf{R} + \boldsymbol{\rho}\mathbf{R}' - \mathbf{R}'\boldsymbol{\rho}' - \boldsymbol{\rho}\mathbf{R}) \right] d^2\boldsymbol{\rho}' d^2\mathbf{R}', \tag{2.12}$$

where

$$F_\xi(\mathbf{R}', \boldsymbol{\rho}') \equiv \langle \exp[i\xi_s(\mathbf{R}' + \boldsymbol{\rho}'/2) - i\xi_s(\mathbf{R}' - \boldsymbol{\rho}'/2)] \rangle. \tag{2.13}$$

For simplicity, we have eliminated the limits of integration. In all cases, integration is performed over the entire (x, y) plane unless defined otherwise. We also use a single integral indicator.

Equation (2.12) can be simplified if we assume that $\xi_s(\mathbf{r})$ is a statistically uniform and isotropic random function. In this case, the function (2.13) depends only on the modulus of the difference coordinate $\boldsymbol{\rho}'$, that is

$$F_{\xi}(\mathbf{R}', \boldsymbol{\rho}')=F_{\xi}(\rho')=<\exp[i\xi_s(\mathbf{R}'+\boldsymbol{\rho}'/2)-i\xi_s(\mathbf{R}'-\boldsymbol{\rho}'/2)]>. \quad (2.14)$$

Correlation between the random values $\xi_s(\mathbf{R}'+\boldsymbol{\rho}'/2)$ and $\xi_s(\mathbf{R}'-\boldsymbol{\rho}'/2)$ in Eq. (2.14) vanishes when the difference coordinate modulus $\rho'=|\boldsymbol{\rho}'|$ exceeds the surface roughness correlation length $\rho'>l_s$. This means that in Eq. (2.12), the function $F_{\xi}(\rho')$ can be assumed as nonzero only inside the integration area $\rho'<l_s$. Note that any potential difference between the characteristic correlation lengths for the random functions $\xi_s(\mathbf{r})$ and $\xi(\mathbf{r})$ is considered small and ignored.

The functions $\tilde{\psi}_T(\mathbf{R}'+\boldsymbol{\rho}'/2)$ and $\tilde{\psi}_T(\mathbf{R}'-\boldsymbol{\rho}'/2)$ in Eq. (2.12) can be considered only inside the area, which is essential for integration over the variable $\boldsymbol{\rho}'$.

The complex amplitude $\tilde{\psi}_T(\mathbf{R}'+\boldsymbol{\rho}'/2)$ in Eq. (2.12) depends on the slowly varying (on the spatial scale $\rho'\sim l_s$) functions $\gamma(\mathbf{R}'+\boldsymbol{\rho}'/2)$, $A_T(\mathbf{R}'\pm\boldsymbol{\rho}'/2)$, and $S(\mathbf{R}'\pm\boldsymbol{\rho}'/2)$ [see Eq. (2.8)]. Inside the area $\rho'\le l_s$, the first two functions can be approximated by using the first terms in the Taylor series expansions: $\gamma(\mathbf{R}'\pm\boldsymbol{\rho}'/2)\approx\gamma(\mathbf{R}')$ and $A_T(\mathbf{R}'\pm\boldsymbol{\rho}'/2)\approx A_T(\mathbf{R}')$.

In contrast, in the approximation of function $S(\mathbf{R}'\pm\boldsymbol{\rho}'/2)$, we keep the first two terms $S(\mathbf{R}'\pm\boldsymbol{\rho}'/2)\approx S(\mathbf{R}')\pm\boldsymbol{\rho}'\nabla S(\mathbf{R}')/2$, as the term $k\boldsymbol{\rho}'\nabla S(\mathbf{R}')/2$ can be nonzero even inside the area of size l_s.

We then obtain the following approximation for the function $\tilde{\psi}_T(\mathbf{R}'+\boldsymbol{\rho}'/2)$ in Eq. (2.12)

$$\begin{aligned}\tilde{\psi}_T(\mathbf{R}'+\boldsymbol{\rho}'/2)&=\gamma(\mathbf{R}'+\boldsymbol{\rho}'/2)\exp[ikS(\mathbf{R}'+\boldsymbol{\rho}'/2)]A_T(\mathbf{R}'+\boldsymbol{\rho}'/2)\\&\approx\gamma(\mathbf{R}')\exp\{ik[S(\mathbf{R}')\pm\boldsymbol{\rho}'\nabla S(\mathbf{R}')/2]\}A_T(\mathbf{R}')\\&=\tilde{\psi}_T(\mathbf{R}')\exp[\pm ik\boldsymbol{\rho}'\nabla S(\mathbf{R}')/2].\end{aligned} \quad (2.15)$$

Assume that inside the illuminated target area the gradient $\nabla S(\mathbf{R}')$ in Eq. (2.15) can be approximated by a constant: $\nabla S(\mathbf{R}')\approx\boldsymbol{\alpha}=\text{const}$. This corresponds to a general tilt of the surface by an angle of $|\boldsymbol{\alpha}|$ inside the target hit-spot area. By substituting expressions (2.14) and (2.15) into Eq. (2.12), we obtain

$$\begin{aligned}\Gamma_{\psi}(\boldsymbol{\rho},\mathbf{R},z=0)=|c_0|^2\exp\left[-i\frac{k}{L}(\mathbf{R}\boldsymbol{\rho})\right]\iint|\tilde{\psi}_T(\mathbf{R}')|^2\exp\left[i\frac{k}{L}\boldsymbol{\rho}\mathbf{R}'\right]\\\times\exp(ik\boldsymbol{\alpha}\boldsymbol{\rho}')F_{\xi}(\rho')\exp\left(i\frac{k}{L}\boldsymbol{\rho}'\mathbf{R}\right)\exp\left(i\frac{k}{L}\boldsymbol{\rho}'\mathbf{R}'\right)d^2\boldsymbol{\rho}'d^2\mathbf{R}'.\end{aligned} \quad (2.16)$$

Consider the argument $k\boldsymbol{\rho}'\mathbf{R}'/L$ in the last exponential term of Eq. (2.16) and note that the area essential for integration over the variable $\mathbf{R}'$ coincides with the target hit-spot area of size b_s. Thus, inside both of the areas in Eq. (2.16) essential for integration – the area of size l_s for integration over ρ' and the area of size b_s for integration over $\mathbf{R}'$ – the term $k\boldsymbol{\rho}'\mathbf{R}'/L$ does not exceed its maximum value L_s/L, where $L_s=kl_sb_s$.

Assume that $L_s/L\ll1$, which corresponds to a target located at the distance $L\gg L_s=kl_sb_s$. In this case, the term $\exp(ik\boldsymbol{\rho}'\mathbf{R}'/L)$ in Eq. (2.16) can be replaced by unity. For most TIL propagation scenarios, the condition $L\gg L_s$ is fulfilled. As an estimation, consider λ=1.0 μm, l_s=50 μm, and b_s=0.25 m. For this example, $L_s\approx$80 m.

For propagation distances $L\gg L_s$, the speckle-field MCF (2.16) can be represented in the following form [28]

$$\Gamma_{\psi}(\boldsymbol{\rho},\mathbf{R},z=0)=|c_0|^2\exp\left(-i\frac{k}{L}\mathbf{R}\boldsymbol{\rho}\right)\Phi(\boldsymbol{\rho})\Phi_{\xi}(\mathbf{R}) \quad (2.17)$$

where

$$\begin{aligned}\Phi(\boldsymbol{\rho})&=\int|\tilde{\psi}_T(\mathbf{R}')|^2\exp\left(i\frac{k}{L}\boldsymbol{\rho}\mathbf{R}'\right)d^2\mathbf{R}'\\&=\int\gamma^2(\mathbf{R}')I(\mathbf{R}',L)\exp\left(i\frac{k}{L}\boldsymbol{\rho}\mathbf{R}'\right)d^2\mathbf{R}',\end{aligned} \quad (2.18)$$

$$\Phi_{\xi}(\mathbf{R})=\int\exp(ik\boldsymbol{\alpha}\boldsymbol{\rho})F_{\xi}(\rho)\exp\left(i\frac{k}{L}\boldsymbol{\rho}\mathbf{R}\right)d^2\boldsymbol{\rho}. \quad (2.19)$$

2.7 Speckle-field correlation spatial scales

An important property of the representation (2.17)–(2.19) is that the speckle-field MCF modulus

$$|\Gamma_{\psi}(\boldsymbol{\rho}, \mathbf{R}, z=0)|=|c_0|^2|\Phi(\boldsymbol{\rho})\Phi_{\xi}(\mathbf{R})| \quad (2.20)$$

is a factorized function with respect to the sum $\mathbf{R}=(\mathbf{r}_1+\mathbf{r}_2)/2$ and difference $\boldsymbol{\rho}=(\mathbf{r}_1-\mathbf{r}_2)/2$ coordinates: the function $\Phi(\boldsymbol{\rho})$ depends only on $\boldsymbol{\rho}$, while $\Phi_{\xi}(\mathbf{R})$ is only a function of the coordinate vector $\mathbf{R}$. This means that the function $\Phi(\boldsymbol{\rho})$ alone defines spatial correlation properties of the MCF with respect to the difference coordinate $\boldsymbol{\rho}$, that is, local correlations occurring within the vicinity of the coordinate vector $\mathbf{R}$. The function $\Phi_{\xi}(\mathbf{R})$ describes changes occurring with local correlations when the observation points $\mathbf{r}_1$ and $\mathbf{r}_2$ are relocated without changing the difference vector $\boldsymbol{\rho}$.

Consider the properties of these functions. First, note that $\Phi(\boldsymbol{\rho})$ in Eq. (2.18) is the Fourier transform of the auxiliary function $|\tilde{\psi}_T(\mathbf{R})|^2=\gamma^2(\mathbf{R})I(\mathbf{R},L)$ defined by Eq. (2.8), and hence, the function $\Phi(\boldsymbol{\rho})$ is independent of the statistical properties of the target surface roughness.

We can estimate the characteristic localization area of the function $\Phi(\boldsymbol{\rho})$ – the range of the variable ρ corresponding to nonzero function values. The size of this area can be easily calculated for a target hit spot of size b_s with a Gaussian intensity distribution: $I(\mathbf{R},L)=I_0\exp(-\mathbf{R}^2/b_s^2)$. Assume for simplicity that $\gamma(\mathbf{R})=1$, and from Eq. (2.18), we obtain

$$\Phi(\boldsymbol{\rho})=\Phi_0\exp(-\rho^2/a_{sp}^2),\ \text{where} \tag{2.21}$$

$$a_{sp}=2L/(kb_s)=L\lambda/(\pi b_s) \tag{2.22}$$

and Φ_0 is a constant. For a fixed coordinate $\mathbf{R}$, the MCF (2.20) is localized inside an area of size a_{sp}. This means that the correlation between the speckle-field complex amplitudes at points $\mathbf{r}_1$ and $\mathbf{r}_2$ vanishes if the separation distance between these points $|\mathbf{r}_1-\mathbf{r}_2|$ exceeds $2a_{sp}$. The spatial scale a_{sp} in Eq. (2.21) is commonly used as an estimate of the *speckle-field correlation length*, also called *speckle radius*.

2.8 Average intensity and speckle-field footprint

Consider the properties of the function $\Phi_{\xi}(\mathbf{R})$ as described by expression (2.19). The function $\Phi_{\xi}(\mathbf{R})$ is the Fourier transform of the product of two functions: $\exp(ik\boldsymbol{\alpha}\boldsymbol{\rho}')$ and $F_{\xi}(\boldsymbol{\rho}')$. From the Fourier transform shift theorem, which states that a linear phase shift in the frequency domain [the term $\exp(ik\boldsymbol{\alpha}\boldsymbol{\rho}')$] introduces a translation in the coordinate domain, and from expression (2.19), we obtain

$$\Phi_{\xi}(\mathbf{R}-\mathbf{R}_{\alpha})=\int F_{\xi}(\rho')\exp\left(i\frac{k}{L}\boldsymbol{\rho}'\mathbf{R}\right)d^2\boldsymbol{\rho}', \tag{2.23}$$

where $\mathbf{R}_{\alpha}=\boldsymbol{\alpha}L$ describes a linear shift of the sum coordinate in the receiver plane resulting from a local tilt of the target surface inside the illuminated area.

The speckle-field average intensity distribution $\langle I_{sp}(\mathbf{R})\rangle \equiv\langle I(\mathbf{R},0)\rangle$ at the receiver plane can be obtained by substituting $\boldsymbol{\rho}=0$ into Eq. (2.11) for the MCF:

$$\Gamma_{\psi}(0,\mathbf{R},0)=\langle\psi(\mathbf{R},0)\psi^{*}(\mathbf{R},0)\rangle=\langle I_{sp}(\mathbf{R})\rangle.$$

Correspondingly, from expressions (2.17) and (2.23), we obtain

$$\begin{aligned}\langle I_{sp}(\hat{\mathbf{R}})\rangle&=\Gamma_{\psi}(0,\hat{\mathbf{R}},0)=|c_0|^2\Phi(0)\Phi_{\xi}(\hat{\mathbf{R}})\\&=|c_0|^2\Phi(0)\int F_{\xi}(\rho')\exp\left(i\frac{k}{L}\boldsymbol{\rho}'\hat{\mathbf{R}}\right)d^2\boldsymbol{\rho}',\end{aligned} \tag{2.24}$$

where $\hat{\mathbf{R}}=\mathbf{R}-\mathbf{R}_{\alpha}$ and

$$\Phi(0)=\int\gamma^2(\mathbf{R})I(\mathbf{R},L)d^2\mathbf{R}. \tag{2.25}$$

According to Eqs. (2.24) and (2.25), the speckle-field average intensity $\langle I_{sp}(\mathbf{R})\rangle$ is the result of incoherent summation of the scattered field contributions from all surface elements (summation of intensities).

The average intensity localization area defines the *speckle-field footprint* at the receiver plane. For estimation of the footprint size, consider the function $F_{\xi}(\rho')$ in Eq. (2.24). This function depends on the random phase modulation function $\xi_s(\mathbf{r})=k_z^s(\mathbf{r})\xi(\mathbf{r})$, where $k_z^s(\mathbf{r})$ is a component of the scattering vector $\mathbf{k}^s(\mathbf{r})=\mathbf{k}_{\theta}-\mathbf{k}_{inc}(\mathbf{r})$ [see expressions (2.3), (2.5) and (2.14)].

For simplicity, assume that variations in the incident wave's wavefront slopes at the target surface are small and can be neglected [$\mathbf{k}_{inc}(\mathbf{r})\simeq\mathbf{k}_{inc}$]. We also assume that the target surface is orthogonal to outgoing wave propagation direction, so that $\mathbf{k}_{\theta}=-\mathbf{k}_{inc}\simeq k_z=k$. In this case, $|\mathbf{k}^s|\simeq k_z^s$ and $k_z^s\simeq -2k_z=-2k$. In this approximation, $\xi_s(\mathbf{r})=-2k\xi(\mathbf{r})$.

Consider the surface roughness profile $\xi(\mathbf{r})$, which can be described by a Gaussian random process (*Gaussian rough surface*). For this case, expression (2.14) can be represented as [20, 27]

$$\begin{aligned}F_{\xi}(\rho')&=\langle\exp[i\xi_s(\mathbf{R}'+\boldsymbol{\rho}'/2)-i\xi_s(\mathbf{R}'-\boldsymbol{\rho}'/2)]\rangle\\&=\exp\{-4k^2\sigma_s^2[1-K_s(\rho')]\},\end{aligned} \tag{2.26}$$

where $K_s(\rho')$ is the Gaussian autocorrelation function with correlation length l_s defined by Eq. (2.2). Inside the region $\rho'\simeq l_s$, the autocorrelation function can be approximated with good accuracy as $K_s(\rho')=\exp[-(\rho')^2/2l_s^2]\simeq 1-(\rho')^2/2l_s^2$. In this case, for $F_{\xi}(\rho')$ in Eq. (2.26), we obtain

$$F_{\xi}(\rho')=\exp\{-4k^2\sigma_s^2[1-K_s(\rho')]\}\simeq\exp[-2(k\theta_s\rho')^2], \tag{2.27}$$

where $\theta_s=\sigma_s/l_s$ is the characteristic angle for the rough surface slopes.

Substituting Eq. (2.27) into Eq. (2.24) results in

$$\langle I_{sp}(\mathbf{R}-\mathbf{R}_{\alpha})\rangle\equiv\langle I(\mathbf{R}-\mathbf{R}_{\alpha},0)\rangle=c_{\alpha}\Phi(0)\exp\left[-\frac{|\mathbf{R}-\mathbf{R}_{\alpha}|^2}{(L\theta_I)^2}\right], \tag{2.28}$$

where $c_{\alpha}=|c_0|^2$, and $\theta_I=2\sqrt{2}\theta_s=2\sqrt{2}(\sigma_s/l_s)$. The distance

$$R_{\psi}=L\theta_I=2\sqrt{2}\theta_sL=2\sqrt{2}(\sigma_s/l_s)L, \tag{2.29}$$

describes the characteristic radius for the average intensity localization area in the receiver plane, and can be referred to as the *speckle-field footprint* radius. Correspondingly, the speckle-field footprint size (diameter) is given by $D_{\psi}=2R_{\psi}$.

It is convenient to represent the average intensity (2.28) as a function of the scattering angle vector $\boldsymbol{\theta}=\mathbf{R}/L$:

$$\langle I_{sp}(\boldsymbol{\theta}\text{-}\boldsymbol{\alpha})\rangle = c_{\alpha}\Phi(0)\exp(-|\boldsymbol{\theta}\text{-}\boldsymbol{\alpha}|^2/\theta_I^2). \tag{2.30}$$

This expression describes the angular distribution of the speckle-field average intensity, and the parameter $\theta_I=2\sqrt{2\theta_s}$ in Eq. (2.30) characterizes the *speckle-field angular width* (half-angle). Note that θ_I depends only on surface roughness characteristics (ratio σ_s/l_s).

A more general analysis shows that the average speckle-field intensity in the selected angular direction $\boldsymbol{\theta}$ is proportional to the probability $W(\nabla\xi)$ of the surface roughness slopes $\nabla\xi$ for which scattering in the direction $\boldsymbol{\theta}$ corresponds to specular reflection: $\nabla\xi(\mathbf{r})=-\mathbf{k}_{\perp}^{s}(\mathbf{r})/k_z^s$ [17, 20]. Generally speaking, this means that the average intensity angular distribution depends on the incident wave's wavefront phase. Nevertheless, for smooth spatial variations of the phase inside the illuminated area, this dependence is relatively weak and with most TIL applications can be neglected. Similarly, variations of surface curvature (shape) inside the target hit spot result in changes in probability of the surface roughness slopes and, hence, may impact the average intensity angular distribution [20, 29].

On the contrary, the surface roughness statistics, as well as the incident wave spatial phase modulation (aberrations) at the target surface and the surface shape, have practically no impact on the speckle-field correlation length a_{sp}. Spatial correlation properties of the speckle-field depend exclusively on the outgoing wave's intensity distribution on the target surface. This property of speckle fields can be used for image quality analysis and adaptive imaging [30, 31].

2.9 Van Cittert-Zernike theorem

Compare the characteristic width of the average intensity angular distribution $\theta_I=2\sqrt{2}(\sigma_s/l_s)$ with the angular speckle-size defined by $\theta_{sp}=a_{sp}/L$. From Eq. (2.22), we obtain $\theta_{sp}=\lambda/(\pi b_s)$. The ratio $\theta_I/\theta_{sp}\simeq 10(b_s/\lambda)\theta_s$ of these two characteristic angular scales of the speckle-field MCF is enormously large. For a typical example where λ=1.0 μm, θ_s=0.1, and b_s=0.25 m, we obtain $\theta_s\simeq$0.3 rad. and $\theta_I/\theta_{sp}=2.3\cdot 10^5$. For the propagation distance L=1.0 km, the beam footprint size is $R_{\psi}=L\theta_I\simeq$300 m, and the characteristic speckle size is given by $a_{sp}\simeq$1.3 mm. Compare the beam footprint size and the speckle size with the receiver telescope aperture size (diameter) D. For D=1.0 m, we have $R_{\psi}=100D$, and $D=770a_{sp}$.

This example shows that for a large size region of the receiver plane Ω, which significantly exceeds the TIL system receiver telescope aperture and contains a large number of speckles, the function $\Phi_{\xi}(\mathbf{R})$ in Eq. (2.17) can be considered as a constant: $\Phi_{\xi}(\mathbf{R})\simeq$const. For a target surface tilted by the angle α, $\Phi_{\xi}(\mathbf{R})\simeq\Phi_{\xi}(\mathbf{R}_{\alpha})$=const.

By substituting this approximation and Eq. (2.18) for the function $\Phi(\boldsymbol{\rho})$ into expression (2.17) for the mutual correlation function, we have

$$\Gamma_{\psi}(\boldsymbol{\rho},\mathbf{R},0)=\frac{k^2}{(2\pi L)^2}\exp\left(-i\frac{k}{L}\mathbf{R}\boldsymbol{\rho}\right)\Phi_{\xi}(\mathbf{R}_{\alpha})\times \int\gamma^2(\mathbf{r})I(\mathbf{r},L)\exp\left(i\frac{k}{L}\boldsymbol{\rho}\mathbf{r}\right)d^2\mathbf{r}. \tag{2.31}$$

For $\gamma(\mathbf{r})$=const and $\mathbf{R}_{\alpha}$=0, this formula coincides with the expression for the well-known *Van Cittert-Zernike theorem* describing the evolution of the mutual coherence function for an optical wave originating from an incoherent light source with intensity distribution $I(\mathbf{r}, L)$ [20, 27].

Assuming $\mathbf{R}_{\alpha}$=0 (orthogonal to the optical axis surface), from Eq. (2.31) for the average intensity, we obtain

$$\langle I_{sp}(\mathbf{r})\rangle=\frac{k^2}{(2\pi L)^2}\int\gamma^2(\mathbf{r}')I(\mathbf{r}',L)d^2\mathbf{r}'. \tag{2.32}$$

The integral (2.32) describes the formation of the speckle-field average intensity as a process of incoherent summation of scattered field contributions from many surface elements. From Eq. (2.32), it also follows that in this approximation, the speckle-field average intensity is a constant: $\langle I_{sp}(\mathbf{r})\rangle=\bar{I}_{sp}$=const.

Using two-dimensional Fourier transforms and Eq. (2.31), represent the MCF modulus in the form

$$|\Gamma_{\psi}(\mathbf{q},\mathbf{R},0)|=\frac{k^2}{(2\pi L)^2}|\Phi_{\xi}(\mathbf{R}_{\alpha})\mathrm{I}_{\psi}(\mathbf{q},L)|, \tag{2.33}$$

where $\mathbf{q}=(k/L)\boldsymbol{\rho}=k\boldsymbol{\theta}$ is the transversal vector in the spectral domain, and $\mathbf{I}(\mathbf{q}, L)$ is the spectral amplitude of the function $|\tilde{\psi}_T(\mathbf{r})|^2=\gamma^2(\mathbf{r})I(\mathbf{r},L)$.

It follows from the Van Cittert-Zernike theorem (2.31), (2.33), that for an extended target with uniform attenuation [$\gamma(\mathbf{r})$=const], the speckle-field MCF, and hence, the speckle-field spatial correlation length a_{sp} are solely dependent on the incident wave intensity distribution on the target surface $I_T(\mathbf{r})\equiv\mathrm{I}(\mathbf{r}, L)$. For a Gaussian intensity of width b_s, the length a_{sp} (speckle-size) is simply inversely proportional to b_s [see Eq. (2.22)].

3 Target-in-the-loop beam quality metrics

3.1 Target-plane beam quality metrics

The spatial correlation properties of speckle fields described above can be used in *adaptive TIL laser beam projection* (*directed energy) systems* [14, 32, 33]. These systems are designed to create a hit spot of the smallest possible size on a remotely located target and, thus, increase the laser beam power density (hit-spot brightness) on the target surface [34]. The desired increase in the hit-spot brightness can be achieved by actively (adaptively) controlling (preshaping) the outgoing wave phase at the TIL system transmitter aperture.

This phase control can be based on optimization of a selected measure (metric) $J_T=J[I_T(\mathbf{r})]$ that characterizes the 'quality' of the target hit-spot intensity distribution $I_T(\mathbf{r})$ (*target-plane beam quality metric*) through the use of various metric optimization techniques [13, 14, 32, 35–38]. Note that these wavefront control techniques can only be applied to TIL laser beam projection systems that operate over relatively short propagation paths, so that the time delay $\tau_d=2L/c$ associated with TIL propagation can be neglected ($\tau_d<\tau_{AO}$).

The same general requirements for the desired target-plane intensity distribution can be described using different metrics. For example, an increase in laser beam energy density on the target surface can be achieved by maximizing the target-plane metric known as the sharpness function [39]

$$J_2=\int I_T^2(\mathbf{r})d^2\mathbf{r}, \tag{3.1}$$

or by minimizing the metric

$$b_s^2=\frac{1}{W_0}\int I_T(\mathbf{r})|\mathbf{r}\text{-}\mathbf{r}_c|^2 d^2\mathbf{r}, \tag{3.2}$$

which characterizes the target hit-spot width b_s. Here,

$$\mathbf{r}_c=\frac{1}{W_0}\int I_T(\mathbf{r})\mathbf{r}d^2\mathbf{r} \quad \text{and} \quad W_0=\int I_T(\mathbf{r})d^2\mathbf{r}, \tag{3.3}$$

where $\mathbf{r}_c$ is the beam centroid vector, and W_0 is the total beam power.

3.2 Receiver-plane metrics: basic requirements

The problem with wavefront control techniques based on target-plane beam quality metric optimization is that in TIL propagation geometry, the target-plane intensity $I_T(\mathbf{r})$ in Eqs. (3.1)–(3.3) cannot be directly measured. Estimation of the beam quality at the target surface can only be performed using measurements of the return field characteristics at the receiver aperture (plane z=0) – *receiver-plane metrics*.

Note that the return speckle-field amplitude at the receiver plane $\psi(\mathbf{r}, z=0)$ is a random function. It depends on many factors including the target-plane field intensity $I_T(\mathbf{r})$ and phase $\phi_T(\mathbf{r})$ distributions, instantaneous realizations of the target surface roughness $\xi(\mathbf{r})$, and the target orientation, shape, and reflection coefficient inside the illuminated area [as described by the functions $\gamma(\mathbf{r})$ and $S(\mathbf{r})$ in Eq. (2.5)].

The questions to be answered are first, what kind of speckle-field characteristics should be measured; and second, how should these characteristics be processed to 'filter' undesirable dependencies of the speckle field on the factors mentioned above to obtain a measure $J_{sp}=J_{sp}[\psi(\mathbf{r}, z=0)]$ (speckle-field based metric) that depends solely on the target-plane intensity distribution $I_T(\mathbf{r})$ and can be used instead of target-plane beam quality metrics.

The measure J_{sp}, referred to as a *speckle-field based beam quality metric* or just *speckle metric*, can be used as a performance metric for adaptive wavefront control in TIL laser beam projection systems if the following conditions are fulfilled: (a) J_{sp} can be computed based on measurements of the speckle-field characteristics at the receiver aperture; (b) J_{sp} monotonically depends on the selected target-plane beam quality metric J_T, and (c) both the speckle-field measurements and computations of J_{sp} can be performed over a time τ_J that is shorter than the characteristic time τ_T for which the hit-spot intensity distribution can be considered stationary ('frozen').

Target plane intensity variations typically result from either atmospheric turbulence-induced beam intensity fluctuations (scintillations) with a characteristic time τ_{at} or from adaptive optics-induced outgoing wave phase modulations with the characteristic time constant τ_{AO}.

3.3 Speckle-average power-in-the-bucket metric

The simplest example of a speckle metric is the *speckle-average power-in-the-bucket* metric $\langle J_{PIB}\rangle$

$$\langle J_{PIB}\rangle=\int_{S_R}\langle|\psi(\mathbf{r},z=0)|^2\rangle d^2\mathbf{r}=\int_{S_R}\langle I_{sp}(\mathbf{r})\rangle d^2\mathbf{r}, \tag{3.4}$$

where S_R is the receiver telescope aperture area and $I_{sp}(\mathbf{r})\equiv I(\mathbf{r}, 0)$ is the return-wave (speckle-field) intensity

distribution. The metric $\langle J_{PIB}\rangle$ can be measured using a receiver telescope with a large-area single photodetector in its focal plane. The metric (3.4) depends on the ensemble-average speckle-field intensity distribution $\langle I_{sp}(\mathbf{r})\rangle$. In most practical cases, the speckle-field beam footprint size D_{ψ} as defined by Eq. (2.29) significantly exceeds the receiver telescope aperture size D, and hence, the average intensity $\langle I_{sp}(\mathbf{r})\rangle$ in Eq. (3.4) can be considered independent of the vector $\mathbf{r}$: $\langle I_{sp}(\mathbf{r})\rangle=\overline{I}_{sp}=\text{const}$.

For a Gaussian surface orthogonal to the optical axis, from Eqs. (2.24), (2.25), and (2.28), we have (with accuracy to a constant insignificant for our analysis)

$$\langle J_{PIB}\rangle=S_R\overline{I}_{sp}=S_R\int\gamma^2(\mathbf{r})I_T(\mathbf{r})d^2\mathbf{r}. \tag{3.5}$$

The metric (3.5) depends solely on the target-plane intensity distribution and, thus, formally satisfies the first speckle-metric requirement introduced above.

Let us examine if this metric can characterize the target hit-spot brightness and, hence, satisfy the second speckle-metric requirement. For an extended target with uniform reflectivity coefficient [$\gamma(\mathbf{r})$=const], the integral in Eq. (3.5) is proportional to the outgoing beam's total power W_0 and, hence, does not depend on the target plane intensity distribution. Accordingly, for extended targets that significantly exceed the hit-spot beam size and have uniform reflectivity (no glints) – a so-called *resolved target* – the speckle-average *power-in-the-bucket (PIB) metric cannot serve as a speckle-metric* and, hence, cannot be used for control of the outgoing beam phase.

For the opposite case of an *unresolved target* – a small target, or a target with an unresolved bright glint for which $\gamma(\mathbf{r})=\delta(\mathbf{r}\text{-}\mathbf{r}_g)$, where $\mathbf{r}_g$ is the target/glint coordinate vector – the PIB metric is proportional to the outgoing beam intensity on the target or glint point: $\langle J_{PIB}\rangle\sim I_T(\mathbf{r}_g)$. For unresolved targets, the measure $J_T=I_T(\mathbf{r}_g)$ represents a target-plane beam quality metric whose value monothonically increases with an increase in the laser beam power density on the small target or target glint. Thus, for unresolved targets, the metric $\langle J_{PIB}\rangle$ satisfies the second speckle-metric requirement ($\langle J_{PIB}\rangle\sim J_T$), and maximization of this metric leads to increases in target hit-spot brightness [38].

For intermediate cases where the size of a resolved target is on the order of the target hit-spot beam size b_s, the PIB metric (3.5) can be used as speckle-metric only during the initial stages of adaptive wavefront phase control. This means that use of metric (3.5) for adaptive wavefront control can only result in partial improvement of the hit-spot brightness.

3.4 Speckle-metric measurements

Assume that the target surface and laser beam are moving with respect to each other in a direction orthogonal to the TIL system optical axis with a linear velocity of v_s. The characteristic time of complete surface roughness realization update can then be estimated by $\tau_s\simeq b_s/v_s$, where b_s is characteristic beam size on the target surface. For computing speckle-average metrics such as $\langle J_{PIB}\rangle$, assume that ensemble averaging can be replaced by time averaging of a sufficiently large number M_{sp} of instantaneous speckle-field intensity distributions $I_{sp}(\mathbf{r}, t_m)$, m=1, …, M_{sp} corresponding to different surface roughness realizations. (This corresponds to the ergodicity assumption.) Speckle patterns are captured at the moments $t_m=m\Delta$, where Δ is the time interval between subsequent measurements. The receiver system photo-array integration time τ_{ph} is assumed sufficiently short to obtain instantaneous ('frozen') intensity snapshots.

In order to obtain statistically independent speckle-pattern realizations, the time interval Δ between subsequent measurements should exceed τ_s, that is $\Delta>b_s/v_s$. Correspondingly, the total time required for the speckle metric measurement is $\tau_J=M_{sp}\Delta>M_{sp}(b_s/v_s)$. Because speckle metrics should be estimated faster than the characteristic time for the changes in the propagation medium's optical inhomogeneities and laser beam wavefront phase, for atmospheric TIL systems, the measurement time τ_J should be significantly shorter than both the characteristic atmospheric time τ_{at} and adaptive optics system response time τ_{AO}, that is, $\tau_J\ll\tau_{AO}\ll\tau_{at}$. This leads to the following requirement: $v_s\gg M_{sp}b_s/\tau_{at}$. As an example, assume b_s=10 cm, $\tau_{at}=5\cdot10^{-3}$ s and M_{sp}=25. This gives v_s>500 m/s. This simple analysis shows that obtaining speckle-metric by capturing a time sequence of speckle patterns is only possible for extremely fast moving (or spinning) targets. In practice, to obtain speckle averaging, even partial surface roughness realization update can be sufficient so that the target surface motion velocity could be up to an order of magnitude less ($v_s\geq$50 m/s in the example considered).

For targets with static or slowly moving (quasistatic) surface motion, speckle averaging can be performed by using artificially induced small-amplitude fast steering (dithering) of the outgoing beam that provides rapid shifts in the target hit spot over distances exceeding the beam size b_s, thus, updating the surface roughness realization inside the illuminated area [12, 33]. Note that fulfilling the speckle-averaging condition $\tau_s\ll\tau_J\ll\tau_{AO}\ll\tau_{at}$ requires tip and tilt modulation of the outgoing beam wavefront phase with dithering frequencies, $\omega_{dith}\sim1/\tau_s$, in the 10-MHz

range, which cannot be achieved using conventional optomechanical beam-steering mirrors.

The required hit-spot dithering frequency can nevertheless be realized by using laser transmitters based on phased fiber array as shown in Figure 4A [33]. This laser beam transmitter (beam director) is composed of densely packed fiber collimators that are optically coupled with a narrow-linewidth multichannel master oscillator power amplifier (MOPA) system that utilizes single-mode polarization maintaining fibers [40–42]. Each channel of the MOPA system includes a $LiNbO_3$ fiber-integrated phase shifter capable of GHz-rate control of the piston phase of the beam transmitted through its corresponding fiber collimator. The high-frequency hit-spot dithering required for speckle metric measurements can be achieved in this system using a piston-wise (stair-mode) approximation of the outgoing beam wavefront tilts as illustrated by the inset at the right top corner in Figure 4B. Note that dithering of the outgoing beam also results in an undesired overall increase of the projected beam's long-exposure hit-spot footprint and the corresponding decrease of the time-averaged power density. For this reason, the stair-mode dithering amplitude should be small, but still large enough to provide a statistically representative ensemble of uncorrelated (or at least weakly correlated) speckle-field realizations that can be used for speckle-metric evaluation. A small dithering amplitude is also important for mitigation of anisoplanatic effects [12].

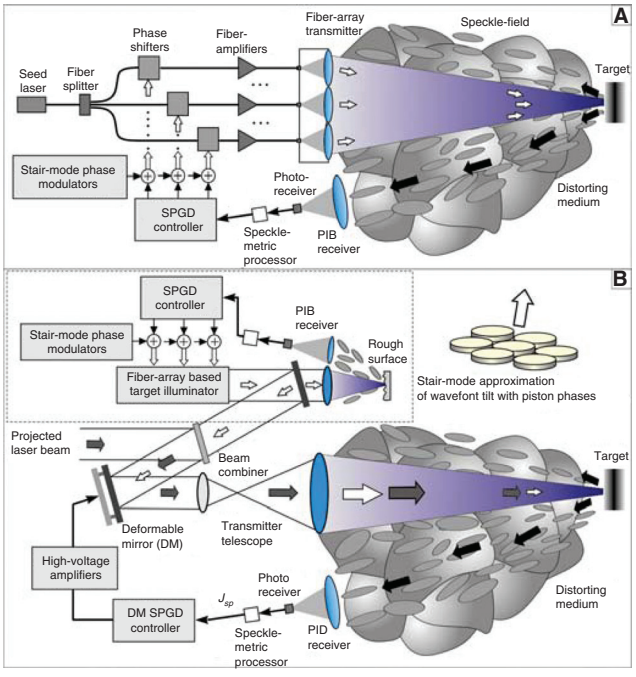

Figure 4 Laser beam projected systems based on adaptive wavefront control using stochastic parallel gradient descent (SPGD) optimization of speckle metrics: (A) fiber-array laser transmitter and (B) conventional beam projection system with fiber-array-based target illuminator (shown inside dashed box).

Owing to the high bandwidth of the fiber-integrated phase shifters, they can be used for both hit-spot dithering and speckle-metric optimization leading to coherent combining (phasing) of the outgoing beams at the target plane. This fiber-array beam projection system with speckle-metric based adaptive wavefront control is shown in Figure 4A. Speckle metric optimization in this system is performed using the stochastic parallel gradient descent (SPGD) control algorithm [43, 44]. In a beam projection system with a conventional laser transmitter telescope as shown in Figure 4B, the phased fiber array is utilized as a target illuminator that uses hit-spot dithering solely for speckle-metric sensing. Speckle metric optimization in this adaptive optics system is achieved by shaping the outgoing beam wavefront phase with a deformable mirror (DM) that is located in the common optical train for both the target illuminator and the projected laser beams. For efficient combining of these beams before entering the transmitter telescope, they should have slightly different wavelengths or orthogonal polarization states. For compensation of the MOPA system-induced random phase shifts in the fiber-array illuminator in Figure 4B, the outgoing beams should be phased at the pupil plane, which can be achieved with an additional speckle metric AO control system shown inside the dashed box in Figure 4B. This control system optimizes the local speckle-metric J_{sp}^{loc}, which is obtained by focusing a small portion of the illuminator beam onto a rough surface.

A different approach to speckle metric measurements is based on sensing in parallel the speckle-field intensity distributions inside the non-overlapping areas $\{\Omega_m\}$, (m=1, …, M_s) belonging to a single large-area speckle-field realization. The speckle-field intensity distributions inside these areas are assumed uncorrelated.

Note that in expression (2.31), the speckle-field MCF $|\Gamma_\psi(\rho, \mathbf{R}, 0)|$ is practically independent of the sum coordinate vector $\mathbf{R}$. This means that speckle-field realizations inside non-overlapping areas $\{\Omega_m\}$, separated by distances of speckle size a_{sp} or larger, can be considered as statistically independent. Sensing of the speckle-field intensity distributions in the areas $\{\Omega_m\}$ can be performed by either using a high-resolution photo-array that captures the large-area speckle-field intensity pattern or by using an array of M_{sp} operating in parallel speckle metric sensors. In this 'space-averaging' approach, the corresponding requirement on the speed of mutual displacement of target surface and laser hit spot is M_{sp} times less restricted ($v_s > b_s/\tau_{at}$).

3.5 Speckle size-based beam quality metrics

The characteristic speckle-field correlation length (speckle size) a_{sp} represents another example of speckle metric referred to here as a *speckle-size metric* [15, 32, 45, 46]. In accordance with the Van Cittert-Zernike theorem (2.33), the correlation length a_{sp} depends on the characteristic target hit-spot size b_s. Increasing the speckle size leads to the desired decrease in target hit-spot size.

The 'true' (MTF-based) estimation of the correlation length a_{sp} requires computationally expensive statistical analysis of speckle-field intensity patterns that are difficult (if even possible) to perform within a relatively short time $\tau_J<\tau_{AO}<\tau_{at}$. Here, we do not distinguish between the spatial correlation lengths associated with the speckle field and the speckle-field intensity. This difference is insignificant for beam quality metric analysis. On the other hand, for the purpose of controlling the outgoing beam phase, the 'true' value of the correlation distance a_{sp} can be replaced by any other characteristic (metric) $J_{sp}=J_{sp}(a_{sp})$ that depends on the 'true' speckle size a_{sp}, but is more convenient for measurements or computations.

Consider an example of such a metric based on indirect speckle-size estimation using computation of speckle pattern edges [15]. Assume that the registered speckle-field intensity distribution $I_{sp}(\mathbf{r})$ (speckle image) contains a large number of speckles. Examples of these types of speckle images, along with the TIL system prototype used for their capturing, are shown in Figure 5.

Consider image processing of speckle-intensity distribution, referred to as edge detection of speckle images. The edge detection can be performed using various techniques: digital, parallel optoelectronic, or on-chip electronic edge processing. Regardless of the technique used, edge detection can be described by an edge-detector operator E applied to the speckle-field intensity $I_{sp}(\mathbf{r})$, resulting in the 'edge-image' $j_e(\mathbf{r})=E[I_{sp}(\mathbf{r})]$. Figure 5 shows examples of speckle-pattern edge processing. Edge images B and D are computed using the digital gradient Sobol operator ∇ applied to the binarized speckle-intensity patterns $I_{sp}^{bin}(\mathbf{r})=sign[I_{sp}(\mathbf{r})-\bar{I}_{sp}]$, where $\bar{I}_{sp}$ is a selected intensity threshold level corresponding to the aperture-average (mean) speckle-field intensity value. The sign function is used to enhance the speckle pattern contrast. In this example, the edge-detector operator can be represented in the form $E[I_{sp}(\mathbf{r})]=|\nabla I_{sp}^{bin}(\mathbf{r})|^2$.

By integrating the edge image $j_e(\mathbf{r})$ over the receiver aperture area S_R, we can obtain a characteristic that is sensitive to the averaged speckle size (speckle-size metric) [15]

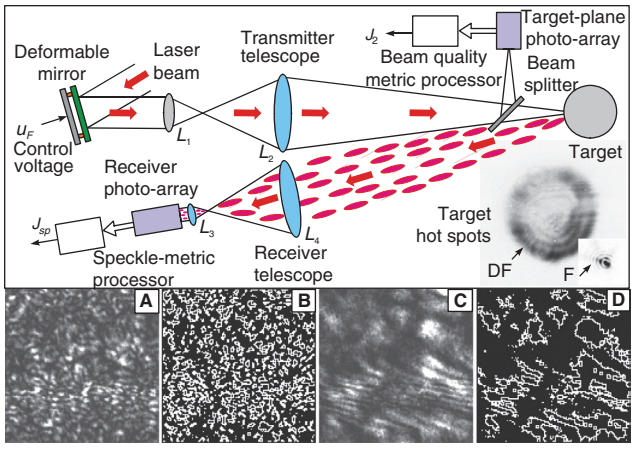

Figure 5 TIL system model for speckle-metric analysis [15]. The photos DF and F are captured by the target-plane photo-array and correspond to the defocused and focused laser beams on the target surface. The bottom photos are speckle-field intensity distributions registered by the receiver [(A) and (C)] and the corresponding edge images [(B) and (D)]. Speckle pattern (A) and edge image (B) correspond to the defocused beam DF; speckle pattern (C) and edge image (D) correspond to the focused beam F. The receiver and target-plane cameras are synchronized to allow simultaneous measurements of the speckle and target-plane intensity distributions used for computation of the speckle-size metric J_{sp} and the target-plane metric J_2, correspondingly. The metric J_{sp} computation time τ_J≈0.01 s. An aluminum half-sphere ~5.0 cm in diameter is used as an extended target. The laser wavelength is 0.514 μm. The optical relay (lenses L_1 and L_2) is used to expand the input beam from 10 mm to 80 mm in diameter. The second optical relay (lenses L_3 and L_4) is used for speckle-pattern scaling.

$$J_{sp}\equiv\int_{S_R} j_e(\mathbf{r})d^2\mathbf{r}=\int_{S_R} E[I_{sp}(\mathbf{r})]\,d^2\mathbf{r}. \tag{3.6}$$

To illustrate the physical meaning of the speckle-size metric (3.6), consider the edge images in Figure 5B and D. These edge images are composed of speckle contours so that the metric J_{sp} in Eq. (3.6) represents the total contribution of edges within a registered speckle pattern. Having a defocused beam on the object surface (as shown by photo *DF*) corresponds to a small characteristic speckle size at the receiver aperture as in Figure 5A and a dense edge-image pattern as in Figure 5B and a larger J_{sp} value. In contrast, the sharply focused beam (photo *F*) corresponds to the large speckles in C, the sparse edge image D, and a small J_{sp}.

Consider a more detailed analysis of dependence of the speckle-size metric (3.6) on the laser beam size at the extended target for the TIL system shown in Figure 5 [15]. In the experiments, the size of the laser beam hit spot on the target surface b_s was controlled by applying control voltage u_F to a deformable mirror incorporated into the transmitter telescope.

For measurement of intensity distribution $I_T(\mathbf{r})$ on the target surface, a portion of the outgoing beam was directed by the beam splitter to the target-plane photo-array (CCD camera) placed in a plane conjugate to the target surface, as shown in Figure 5. The intensity $I_T(\mathbf{r})$ was used to calculate the target-plane beam quality metric (sharpness function) J_2 using expression (3.1). The scattered off-the-target surface speckle field propagated to the receiver telescope located near the transmitter system.

By continuously changing the control voltage u_F applied to the deformable mirror electrodes, the beam size on the target was varied from highly defocused ($b_s \simeq 5.0$ mm) as shown in photo *DF* in Figure 5, to sharply focused in photo *F* ($b_s \simeq 0.2$ mm). Further increases in the control voltage resulted in the laser beam focusing on planes located in front of the target, with a corresponding monotonic increase in the target-plane beam size.

Dependence of the target-plane metric J_2 [Eq. (3.1)], speckle-size metric J_{sp} [Eq. (3.6)], and the speckle average power-in-the-bucket metric $\langle J_{PIB} \rangle$ [Eq. (3.4)] on changes in the control voltage are shown in Figure 6. Both J_2 and J_{sp} metrics have their extrema (maximum for J_2 and minimum for J_{sp}) at approximately the same voltage corresponding to the smallest possible beam size on the target surface, while metric $\langle J_{PIB} \rangle$ is practically insensitive to the target beam size.

The presence of well-localized single extrema on the speckle-size metric curve that coincide with the extremum for the target-plane metric is exactly the property of the speckle-based metric required for adaptive control in TIL projection systems.

In closed-loop experiments with an adaptive TIL system prototype (in a setting similar to that shown in Figure 6), utilization of the speckle-size metric J_{sp} for the outgoing beam adaptive wavefront control resulted in significant improvement of hit-spot brightness on the extended target surface [15]. Note that adaptive control based on the speckle-average PIB metric $\langle J_{PIB} \rangle$ [Eq. (3.4)] failed to increase the target hit-spot brightness. The TIL speckle-size metric optimization system was able to operate with a strongly defocused beam where the initial hit-spot size exceeded its minimum size by nearly 20 times. In these scenarios, adaptive beam control using the target-plane metric J_2 was unstable and required an initial beam prefocusing. At the same time, the beam size on the target achieved by optimizing metric J_2 was nearly diffraction-limited, while for the speckle metric, it was three to five times larger. Note that it is impossible to use the target-plane metric in actual TIL systems because of the absence of information [target-plane intensity $I_T(\mathbf{r})$] required for J_2 metric computation. Here, the metric J_2 was only used for purposes of analyzing speckle-metric efficiency.

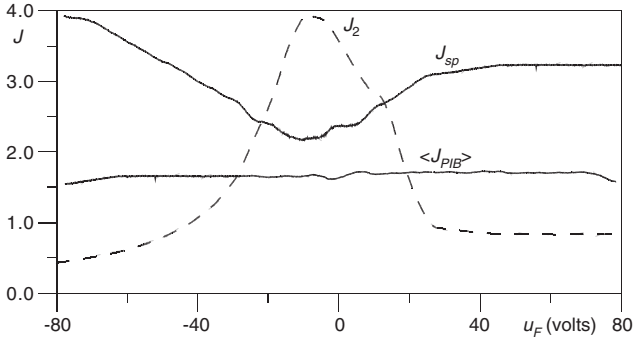

Figure 6 Normalized beam quality metrics *J*, where *J* is either the target-plane metric J_2, or the speckle-size metric J_{sp}, or the average PIB metric $\langle J_{PIB} \rangle$, vs. controlling voltage u_F applied to the deformable mirror in the TIL beam projection system shown in Figure 5. Beam size on the target changed from $b_s \simeq 5.0$ mm (u_F=-80 V) to the sharply focused beam with $b_s \simeq 0.2$ mm for u_F=-8 V and further to the highly defocused beam $b_s \simeq 7.0$ mm (u_F=-80 V) with the indicated control voltage change.

This behavior of the closed-loop adaptive optics system can be understood through analysis of the metric curve shapes in Figure 6. The sharpness function curve (target-plane metric J_2) has a better localized extremum than does the more shallow minimum for the speckle metric J_{sp}. At the same time, the metric J_{sp} shows sensitivity to the target hit-spot size over a large range of beam sizes corresponding to the control voltage change in Figure 6.

This highlights an important property of speckle metric optimization in target-in-the-loop adaptive systems. These systems work well when there are a number of speckles inside the receiver aperture. While speckle-metric optimization adaptive control reduces the beam size on the object up to the point where there are only a few speckles inside the receiver aperture, it is no longer valid to replace the 'true' ensemble averaging by space averaging for speckle-size metric computation. The use of space averaging in this case leads to an increase of noise in metric measurement. As a result, with speckle-size metric optimization, the beam width on the target can be noticeably larger than the diffraction-limited beam size.

In contrast, conventional adaptive optics is typically efficient exactly under conditions where the target-induced speckles are large (on the order of transceiver aperture size), that allows efficient sensing of wavefront phase aberrations using conventional wavefront sensors. Thus, the speckle-size metric-based adaptive technique can be used for precompensation of phase distortions under conditions of strong speckle modulation (many speckles inside adaptive optics transceiver aperture) where conventional adaptive techniques typically fail. A

combination of conventional and speckle metric-based adaptive techniques may provide effective target-in-the-loop adaptive optical control in the presence of strong speckle-field modulation.

Other approaches to improve the performance of speckle-size-based TIL systems are the use of multiple receiver apertures or large apertures that exceed the transmitter aperture size, so that even with diffraction-limited compensation, the receiver telescope captures a sufficient number of speckles for accurate speckle-metric estimation.

4 Speckle-field intensity fluctuations

4.1 Basic assumptions

In the previous discussion of speckle metrics, we were not entirely consistent in the sense that the introduced beam quality metrics in Section 3 were based on speckle-field intensity measurements, but the physical arguments justifying their use in adaptive wavefront control were based on analysis of correlation properties of the speckle-field complex amplitude – not intensity.

There are two reasons for this inconsistency. First, as we have shown in this section, the spatial correlation properties of the speckle-field complex field and intensity are alike in that both depend similarly on the TIL outgoing wave intensity distribution on the target. Second, rigorous analysis of the correlation properties of speckle-field intensity is a significantly more complicated problem than the corresponding analysis of the speckle-field complex amplitude correlation described.

In addition, to avoid considering the multiple-scattering problem, derivation of the speckle-field MCF in Section 2 was based on the smooth surface assumption, which allowed use of the small-slope approximation leading to a closed-form expression for the speckle-field MCF [Eq. (2.17)–(2.19)].

In this section, we depart from these restrictions and directly consider analysis of spatial and temporal correlation properties of speckle-field intensity fluctuations originating from scattering off very rough surfaces. This analysis is based on qualitative models of the scattering process [47–49]. Here, we highlight some of the physical assumptions that form the basis for these models. The main contribution to the scattered field at the observation point **r** originates from a large number of small target surface areas with centers in the specular reflection points. Correspondingly, the speckle field at each point **r** can be considered as the superposition of waves arriving at **r** from these small surface areas. The summation of these waves occurs incoherently. As a result, the ensemble-average intensity at the observation point **r** is proportional to the integral of the intensity distribution $I_T(\mathbf{r})=I(\mathbf{r}, L)$ over the target surface areas. This incoherent character of intensity summation can be seen in the expression for average intensity [Eq. (2.32)] obtained using the small-slope approximation in Section 2.

Obviously, when the surface roughness slopes (parameter $\theta_s \simeq \sigma_s / l_s$) increase, the number of specular reflection points also increases. In accordance with the central limit theorem, if the number of statistically independent random components forming the optical field complex amplitude is large, the resulting field complex amplitude can be considered normally distributed [21]. This means that the field modulus (amplitude) has a Rayleigh probability distribution, and its phase is uniformly distributed over the interval $[-\pi, \pi]$ [18].

Under this assumption, the angular distribution of the speckle-field average intensity [see Eq. (2.30)] is assumed to be significantly wider than the angular area of the TIL system receiver aperture where the speckle-field statistical properties are considered. These arguments will be applied for analysis of the speckle-field intensity spatio-temporal correlation properties.

4.2 Speckle-field complex amplitude representation

Consider a partitioning of the target surface into the small regions $\{\Omega_l\}$, (l=1, …, N) of area $\delta_s \equiv (dx \cdot dy)$ with centers at points $\{\mathbf{r}_l\}$ and assume that the complex amplitude on the target surface $A_T(\mathbf{r}_l)=A(\mathbf{r}_l, z=L)$ can be approximated inside these regions by the constant values $A_l=A_T(\mathbf{r}_l)$. We also assume that each surface region Ω_l contains a large number of specular reflection points. Correspondingly, at the receiver aperture point ($\mathbf{r}$, z=0), each complex amplitude component $A_l(\mathbf{r}, z=0) \equiv a_l \exp(i\phi_l)$ originating from the corresponding surface region Ω_l is a normally distributed random variable with phase ϕ_l having a uniform probability distribution over the interval $[-\pi, \pi]$ and amplitude a_l with a Rayleigh probability distribution.

The resulting total return-field complex amplitude at the point can be represented in the form

$$\psi(\mathbf{r}, z=0)=\sum_{l=1}^{N} a_l \exp(i\phi_l), = \sum_{l=1}^{N} a_l \exp(i\varphi_l + i\Phi_l), \qquad (4.1)$$

where N is the number of target surface regions $\{\Omega_l\}$. The phase ϕ_l in Eq. (4.1) is represented as the sum of two

components: $\phi_l=\varphi_l+\Phi_l$, where Φ_l is the mean value of ϕ_l. The phase component φ_l is dependent only on the surface roughness random variable and has uniform over $[-\pi, \pi]$ probability distribution and zero mean.

On the contrary, the deterministic phase component Φ_l depends on the outgoing wave phase $\varphi_l^T \equiv \varphi_T(\mathbf{r}_l')$ at the surface region Ω_l central point $(\mathbf{r}_l', z=L)$ and on the phase shift $\varphi(\mathbf{r}_l', \mathbf{r})=kR(\mathbf{r}_l', \mathbf{r})$ related with the optical path length associated with spherical wave propagation from the target-plane point $(\mathbf{r}_l', z=L)$ to the receiver-plane point $(\mathbf{r}, z=0)$. (For simplicity, we assumed the target surface is flat and oriented orthogonally to the optical axis.) This propagation occurs over the distance $R_l \equiv R(\mathbf{r}_l', \mathbf{r})=(L^2+|\mathbf{r}_l'-\mathbf{r}|^2)^{1/2}$.

The phase component Φ_l may also include an additional term $\varphi_l^a \equiv \varphi^a(\mathbf{r}_l', \mathbf{r})$ that accounts for phase aberrations of the spherical wave due to propagating through an optically inhomogeneous medium between these two points. Thus, for the phase Φ_l, we obtain

$$\Phi_l \equiv \Phi_l(\mathbf{r}_l', \mathbf{r})=\varphi_l^T+kR_l+\varphi_l^a= \varphi_T(\mathbf{r}_l')+k(L^2+|\mathbf{r}_l'-\mathbf{r}|^2)^{1/2}+\varphi_a(\mathbf{r}_l', \mathbf{r}). \quad (4.2)$$

In order to associate the amplitudes $\{a_l\}$ in Eq. (4.1) with the outgoing wave complex amplitude at the target surface, consider the expression for the speckle-field average intensity $\langle I_{sp}(\mathbf{r})\rangle \equiv \langle \psi(\mathbf{r},0)\psi^*(\mathbf{r}, 0)\rangle$. Using Eq. (4.1) $\langle I_{sp}(\mathbf{r})\rangle$ can be represented as

$$\langle I_{sp}(\mathbf{r})\rangle \equiv \langle I(\mathbf{r},0)\rangle = \sum_l \sum_m \langle a_l a_m \exp[i(\varphi_l-\varphi_m)+i(\Phi_l-\Phi_m)]\rangle. \quad (4.3)$$

By assuming statistical independence of the random amplitudes and phases, Eq. (4.3) reads

$$\langle I_{sp}(\mathbf{r})\rangle = \sum_l \sum_m \langle a_l a_m\rangle \langle \exp[i(\varphi_l-\varphi_m)]\rangle \exp[i(\Phi_l-\Phi_m)]. \quad (4.4)$$

Note that for the random variables $\{\varphi_l\}$ with probability distribution uniform over $[-\pi, \pi]$ and zero mean, the first exponential term in Eq. (4.4) can be represented in the form

$$\langle \exp[i(\varphi_l-\varphi_m)]\rangle = \delta_{l,m}, \quad (4.5)$$

where $\delta_{l,m}$ is the Kronecker symbol [17].

Expression (4.4) for the average intensity can be simplified by using Eq. (4.5) and the known relationship $\langle a_l^2\rangle = (4/\pi)\langle a_l\rangle^2$ between the mean value and variance for random variables with Rayleigh probability distribution

$$\langle I_{sp}(\mathbf{r})\rangle = (4/\pi)\sum_l \langle a_l\rangle^2. \quad (4.6)$$

Consider expression (2.32) for the speckle-field average intensity obtained with the small-slope approximation. Similar to Eq. (4.6), the integral in this expression can be represented in the form of a sum of contributions corresponding to the small target surface regions $\{\Omega_l\}$

$$\langle I_{sp}(\mathbf{r})\rangle = \frac{k^2}{(2\pi L)^2}\sum_l \gamma^2(\mathbf{r}_l') I(\mathbf{r}_l', L)\delta s. \quad (4.7)$$

Equations (4.6) and (4.7) for the average intensity coincide if we represent the random amplitudes a_l in the form

$$a_l = c\gamma(\mathbf{r}_l')|A(\mathbf{r}_l')|(\delta s)^{1/2}\xi_l, \quad (4.8)$$

where $c=k/(2\pi L)$, and $A(\mathbf{r}_l') \equiv A(\mathbf{r}_l', L)$ is the target-plane complex amplitude at the central point of the target surface region, Ω_l and ξ_l are statistically independent auxiliary random variables with Rayleigh probability distributions and equal mean values (for all l)

$$\langle \xi_l\rangle = \langle \xi_m\rangle = \pi/4, \text{ and } \langle \xi_l^2\rangle = 1. \quad (4.9)$$

4.3 Moving target: speckle-field intensity fluctuations

Assume a target surface moving with a constant velocity $\mathbf{v}_s$ and consider the deviation $\delta I_{sp}(\mathbf{r}_1, t)$ of the scattered field intensity from its average value at the receiver point $(\mathbf{r}_1, L=0)$ resulting from this motion, also referred to as the intensity fluctuation $\delta I_{sp}(\mathbf{r}_1, t)=I_{sp}(\mathbf{r}_1, t)-\langle I_{sp}(\mathbf{r}_1, t)\rangle$. Using Eq. (4.1) and expression (4.8), for the deviation $\delta I_{sp}(\mathbf{r}_1, t=t_1)$, we obtain

$$\delta I_{sp}(\mathbf{r}_1, t_1) = c^2\sum_{l,m}|A(\mathbf{r}_l')||A(\mathbf{r}_m')|\exp[i(\phi_l-\phi_m)]\xi_l\xi_m\delta s - c^2\sum_l |A(\mathbf{r}_l')|^2\delta s. \quad (4.10)$$

To simplify the notation, we have assumed that $\gamma(\mathbf{r}')=1$.

At time $t=t_2=t_1+\tau$, the target surface is displaced by the distance $|\mathbf{v}_s|\tau$. The intensity fluctuation at the receiver point $(\mathbf{r}_2, L=0)$ at $t=t_2$ is given by the expression

$$\delta I_{sp}(\mathbf{r}_2, t_1+\tau) = c^2\sum_{l,m}|A(\mathbf{r}_l'+\mathbf{v}_s\tau)||A(\mathbf{r}_m'+\mathbf{v}_s\tau)|\times \exp[i(\hat{\phi}_l-\hat{\phi}_m)]\hat{\xi}_l\hat{\xi}_m\delta s - c^2\sum_l |A(\mathbf{r}_l'+\mathbf{v}_s\tau)|^2\delta s, \quad (4.11)$$

where $\hat{\varphi}_l=\hat{\varphi}_l+\hat{\Phi}_l$ is the phase component at the observation point $\mathbf{r}_2$ originating from the surface region Ω_l. Because the random variables ξ_l, $\hat{\xi}_l$, and φ_l $\hat{\varphi}_l$ are determined only by surface roughness inside the region Ω_l and do not change with either the surface displacement or observation point relocation, we can assume in Eq. (4.11) that $\hat{\xi}_l=\xi_l$ and $\hat{\varphi}_l=\varphi_l$.

4.4 Speckle-field intensity fluctuations MCF

Consider the spatiotemporal correlation properties of the speckle-field intensity fluctuations. Similar to Eq. (2.9), the mutual correlation function (MCF) for the speckle-field intensity fluctuations can be defined as

$$\Gamma_{\delta I}(\mathbf{r}_1,\mathbf{r}_2,\tau)\equiv<\delta I_{sp}(\mathbf{r}_1,t_1)\delta I_{sp}(\mathbf{r}_2,t_2)>. \tag{4.12}$$

By substituting expressions (4.10) and (4.11) into Eq. (4.12) and taking into account that $\hat{\xi}_l=\xi_l$ and $\hat{\varphi}_l=\varphi_l$, we obtain

$$\Gamma_{\delta I}(\mathbf{r}_1,\mathbf{r}_2,\tau)=c^4\sum_{l\neq m}|A(\mathbf{r}_l')A^*(\mathbf{r}_l'+\mathbf{v}_s\tau)A^*(\mathbf{r}_m')A(\mathbf{r}_m'+\mathbf{v}_s\tau)| \times\exp[i(\Phi_l-\Phi_m)-i(\hat{\Phi}_l-\hat{\Phi}_m)](\delta s)^2. \tag{4.13}$$

In the derivation of this expression, we assumed statistical independence of the random variables ξ_l and φ_l. Also, the properties (4.5), (4.9) of the random variables φ_l and ξ_l were used.

By substituting into Eq. (4.13) expressions for the phases in the form (4.2) and taking into account that $A(\mathbf{r}_l')=|A(\mathbf{r}_l')|\exp(i\varphi_l^T)$, we have

$$\Gamma_{\delta I}(\mathbf{r}_1,\mathbf{r}_2,\tau)=c^4\sum_{l\neq m}A(\mathbf{r}_l')A^*(\mathbf{r}_l'+\mathbf{v}_s\tau)A^*(\mathbf{r}_m')A(\mathbf{r}_m'+\mathbf{v}_s\tau) \times\exp[ik(R_l-R_m)-ik(\hat{R}_l-\hat{R}_m)]\exp(i\Theta_{l,m}^a)(\delta s)^2, \tag{4.14}$$

where $R_l=(L^2+|\mathbf{r}_l'-\mathbf{r}_1|^2)^{1/2}$, $\hat{R}_l=(L^2+|\mathbf{r}_l'+\mathbf{v}_s\tau-\mathbf{r}_2|^2)^{1/2}$, and $\Theta_{l,m}^a=[\varphi_a(\mathbf{r}_l',\mathbf{r}_1)-\varphi_a(\mathbf{r}_m',\mathbf{r}_1)]-[\varphi_a(\mathbf{r}_l'+\mathbf{v}_s\tau,\mathbf{r}_2)-\varphi_a(\mathbf{r}_m'+\mathbf{v}_s\tau,\mathbf{r}_2)]$.

If we assume that the inequality $L>>|\mathbf{r}_l'-\mathbf{r}_1|$ is valid for all target regions $\{\Omega_l\}$ and for all receiver aperture points $\mathbf{r}_1$, the expressions for R_l and $\hat{R}_l$ in Eq. (4.14) can be approximated by the first two terms of the Taylor series expansion: $R_l\simeq L+|\mathbf{r}_l'-\mathbf{r}_1|^2/(2L)$ and $\hat{R}_l\simeq L+|\mathbf{r}_l'+\mathbf{v}_s\tau-\mathbf{r}_2|^2/(2L)$. The first exponential term in Eq. (4.14) can then be replaced by the expression $\exp[-ik\boldsymbol{\rho}_p'(\mathbf{v}_s\tau-\boldsymbol{\rho}_{2,1})/L]$, where $\boldsymbol{\rho}_p'=\mathbf{r}_m'-\mathbf{r}_l'$, $\boldsymbol{\rho}_{2,1}=\mathbf{r}_2-\mathbf{r}_1$, and p is the new summation index.

Using the coordinate vectors $\boldsymbol{\rho}_p'$ and $\mathbf{r}_l'$, Eq. (4.14) can be represented in the form

$$\Gamma_{\delta I}(\mathbf{r}_1,\mathbf{r}_2,\tau)=c^4\sum_p\exp\left[-i\frac{k}{L}\boldsymbol{\rho}_p'(\mathbf{v}_s\tau-\boldsymbol{\rho}_{2,1})\right]\delta s\times \sum_l A(\mathbf{r}_l')A^*(\mathbf{r}_l'-\boldsymbol{\rho}_p')A^*(\mathbf{r}_l'+\mathbf{v}_s\tau)A(\mathbf{r}_l'+\mathbf{v}_s\tau-\boldsymbol{\rho}_p')\exp(i\Theta_{l,p}^a)\delta s. \tag{4.15}$$

By assuming that the surface-illuminated area contains a sufficiently large number of specular reflection points, the summation in Eq. (4.15) can be replaced by integration over the surface area

$$\Gamma_{\delta I}(\mathbf{r}_1,\mathbf{r}_2,\tau)=c^4\int\exp\left[-i\frac{k}{L}\boldsymbol{\rho}'(\mathbf{v}_s\tau-\boldsymbol{\rho})\right]\times\int A_T(\mathbf{r}')A_T^*(\mathbf{r}'-\boldsymbol{\rho}') \times A_T^*(\mathbf{r}'+\mathbf{v}_s\tau)A_T(\mathbf{r}'+\mathbf{v}_s\tau-\boldsymbol{\rho}')\exp(i\Theta_a)d^2\mathbf{r}'d^2\boldsymbol{\rho}', \tag{4.16}$$

where we made the following substitutions: $\rho_{2,1}\to\rho$ and $\boldsymbol{\rho}_p'\to\boldsymbol{\rho}'$. In this expression,

$$\Theta_a=[\varphi_a(\mathbf{r}',\mathbf{r}_1)-\varphi_a(\mathbf{r}'-\boldsymbol{\rho}',\mathbf{r}_1)]-[\varphi_a(\mathbf{r}'+\mathbf{v}_s\tau,\mathbf{r}_2)-\varphi_a(\mathbf{r}'+\mathbf{v}_s\tau-\boldsymbol{\rho}',\mathbf{r}_2)].$$

Expression (4.16) represents the Fourier transform of a convolution integral (internal integral over $d^2\mathbf{r}'$). Using the convolution theorem stating that the Fourier transform of a convolution of two functions is the product of their Fourier transforms, from Eq. (4.16), we obtain

$$\Gamma_{\delta I}(\mathbf{r}_1,\mathbf{r}_2,\tau)=c^4\left|\int A_T(\mathbf{r}')A_T^*(\mathbf{r}'+\mathbf{v}_s\tau)\exp[i\Phi_a(\mathbf{r}',\mathbf{r}_1,\mathbf{r}_2)] \times\exp\left[-i\frac{k}{L}\mathbf{r}'(\mathbf{v}_s\tau-\boldsymbol{\rho})\right]d^2\mathbf{r}'\right|^2 \tag{4.17}$$

where $\Phi_a(\mathbf{r}',\mathbf{r}_1,\mathbf{r}_2)=\varphi_a(\mathbf{r}',\mathbf{r}_1)-\varphi_a(\mathbf{r}'+\mathbf{v}_s\tau,\mathbf{r}_2)$, and $\boldsymbol{\rho}=\mathbf{r}_2-\mathbf{r}_1$.

The spatial mutual correlation function of the speckle-field intensity fluctuations can be obtained by substituting $\tau=0$ into Eq. (4.17)

$$\Gamma_{\delta I}(\mathbf{r}_1,\mathbf{r}_2,0)=c^4\left|\int I_T(\mathbf{r}',L)\exp[i\varphi_a(\mathbf{r}',\mathbf{r}_1)-i\varphi_a(\mathbf{r}',\mathbf{r}_2)] \times\exp\left(i\frac{k}{L}\mathbf{r}'\boldsymbol{\rho}\right)d^2\mathbf{r}'\right|^2, \tag{4.18}$$

where $I_T(\mathbf{r}')=A(\mathbf{r}')A^*(\mathbf{r}')$ is the intensity distribution on the target surface.

The expression for $\Gamma_{\delta I}(\mathbf{r}_1,\mathbf{r}_2,0)$ depends on the instantaneous ('frozen') phase aberration function $\varphi_a(\mathbf{r}',\mathbf{r})$ associated with spherical wave propagation from the target surface point $(\mathbf{r}',L)$ to the receiver aperture point $(\mathbf{r},L)$. For this reason, the function $\Gamma_{\delta I}(\mathbf{r}_1,\mathbf{r}_2,0)$ in Eq. (4.18) can be referred to as the *instantaneous MCF* for the speckle-field intensity fluctuations. The instantaneous MCF

corresponds to ensemble averaging over the target surface roughness realizations (speckle-averaging) for 'frozen' propagation medium optical inhomogeneities.

Consider phase distortions originating from a thin layer of optical inhomogeneities located close to the receiver pupil plane (*pupil-plane phase screen*), as illustrated in Figure 7A.

In this case, the phase aberration function is independent of the coordinate $\mathbf{r}'$ inside the target surface-illuminated area, and hence, $\varphi_a(\mathbf{r}', \mathbf{r}_1)=\varphi_a(\mathbf{r}_1)$. This corresponds to the case of TIL system operation with a so-called *isoplanatic target* (*isoplanatic beacon*). For an isoplanatic beacon, the first exponential term in Eq. (4.18), $\exp[i\phi_a(\mathbf{r}_1)-i\varphi_a(\mathbf{r}_2)]$, does not depend on the integration variable $\mathbf{r}'$ and, hence, has no impact on the MCF.

For the opposite case of a phase screen located near the target plane (*target-plane phase screen*), phase aberrations depend on the target point coordinate rather than on the observation point coordinate, as shown in Figure 7B. In this case, $\varphi_a(\mathbf{r}', \mathbf{r}_1)=\varphi_a(\mathbf{r}', \mathbf{r}_2)$, and similar to the pupil-plane phase screen case, the first exponential term in Eq. (4.18) is unity. Correspondingly, the presence of target-plane phase aberrations has no impact on the spatial correlation properties of the speckle-field intensity fluctuations.

For phase-distorting layers located either at the receiver pupil plane or at the target plane, the expression

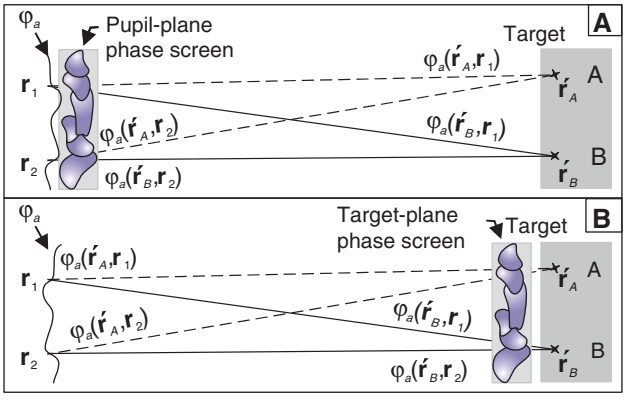

Figure 7 Wave propagation in an optically inhomogeneous medium represented by a thin phase screen located in the receiver plane (A), and in the target plane (B). In (A), phase aberrations corresponding to spherical wave propagation from the target points *A* and *B* to the receiver points $\mathbf{r}_1$ and $\mathbf{r}_2$ are independent of target point location: $\varphi_a(\mathbf{r}'_A,\mathbf{r}_1)=\varphi_a(\mathbf{r}'_A,\mathbf{r}_2)$ and $\varphi_a(\mathbf{r}'_B,\mathbf{r}_1)=\varphi_a(\mathbf{r}'_B,\mathbf{r}_2)$. In (B), the corresponding aberrations are independent of the receiver point: $\varphi_a(\mathbf{r}'_A,\mathbf{r}_1)=\varphi_a(\mathbf{r}'_B,\mathbf{r}_1)$ and $\varphi_a(\mathbf{r}'_A,\mathbf{r}_2)=\varphi_a(\mathbf{r}'_B,\mathbf{r}_2)$. Propagation geometry in (A) corresponds to isoplanatic and in (B) to anisoplanatic conditions. In both TIL propagation scenarios, the presence of phase-distorting layers does not impact the speckle-field intensity mutual correlation function.

for the speckle-field intensity fluctuation MCF (4.18) coincides with the expression for the MCF obtained in an optically homogeneous medium when $\varphi_a(\mathbf{r}', \mathbf{r}_1)=0$:

$$\Gamma_{\delta I}(\boldsymbol{\rho},\tau)=c^4\left|\int A_T(\mathbf{r}')A_T^*(\mathbf{r}''+\mathbf{v}_s\tau)\exp[ik\mathbf{r}'(\mathbf{v}_s\tau-\boldsymbol{\rho})/L]\,d^2\mathbf{r}'\right|^2. \tag{4.19}$$

Note that in this case, the MCF (4.19) only depends on the difference coordinate $\boldsymbol{\rho}=(\mathbf{r}_1-\mathbf{r}_2)$.

The spatial MCF for speckle-field intensity fluctuations in an optically homogeneous medium can be obtained by substituting $\tau=0$ into Eq. (4.19)

$$\Gamma_{\delta I}(\boldsymbol{\rho},0)=c^4\left|\int I(\mathbf{r}',L)\exp\left(i\frac{k}{L}\mathbf{r}'\boldsymbol{\rho}\right)d^2\mathbf{r}'\right|^2. \tag{4.20}$$

Correspondingly, the expression for the variance of the speckle-field intensity fluctuations can be obtained from Eq. (4.20) by considering the case $\boldsymbol{\rho}=0$

$$\sigma_I^2\equiv\Gamma_{\delta I}(0,0)=c^4\left[\int I(\mathbf{r}',L)d^2\mathbf{r}'\right]^2=<I_{sp}(\mathbf{r},L)>^2. \tag{4.21}$$

Here, we used expression (2.32) for the average speckle-field intensity.

It follows from Eq. (4.21) that the intensity fluctuation variance is proportional to the squared average intensity. This speckle-field property is the result of the normal probability distribution assumption for the field complex amplitude.

4.5 Characteristic speckle size

Compare expression (4.20) for the speckle-intensity fluctuation MCF with expression (2.31) for the speckle-field complex amplitude MCF. Both functions are determined by the Fourier transform of the target hit-spot intensity distribution $I_T(\mathbf{r}')\equiv I(\mathbf{r}', L)$, and hence, in both cases, the corresponding spatial correlation lengths are determined by the spectral width of the function $I(\mathbf{r}', L)$. Nevertheless, because in Eq. (4.20) the Fourier integral is squared, the correlation lengths for the speckle-field complex amplitude (speckle-size a_{sp}) and the speckle-intensity fluctuations (speckle-size $\hat{a}_{sp}$) do not coincide.

For a target hit spot with Gaussian intensity distribution of size b_s

$$I_T(\mathbf{r})=I_s\exp(-r^2/b_s^2), \tag{4.22}$$

where I_s is a constant, these correlation lengths are linked by the relationship

$$\hat{a}_{sp}=\frac{1}{2}a_{sp}=\frac{L}{kb_s}. \tag{4.23}$$

As in practice, speckle-size estimation is based on speckle field-intensity measurements, the intensity fluctuation MCF width defines the 'true' speckle size. Note that the characteristic speckle size in Eq. (4.23) have exactly the same dependence on the propagation path length L, beam size b_s, and wavelength (wave number k).

As an example, estimate the characteristic speckle size $\hat{a}_{sp}$ for typical TIL beam projection scenarios. Assume a TIL transmitter system with an outgoing beam having a Gaussian intensity distribution of size a_0 (beam radius) and an extended target located at a distance L from the transmitter aperture. The diffraction-limited (smallest possible) beam size on the target (target hit-spot size) is $b_s^{dif}=L/(ka_0)$.

In accordance with Eq. (4.23), the characteristic speckle size $\hat{a}_{sp}^{dif}=L/(kb_s^{dif})=a_0$. Thus, under optimal laser beam projection conditions, the speckle size is on the order of the transmitter aperture size.

For a collimated outgoing beam, the target hit-spot size $b_s^{col}=a_0[1+(L/L_d)^2]^{1/2}$, where $L_d=ka_0^2$. For short distances ($L<0.5L_d$), the speckle size can be approximated by $\hat{a}_{sp}^{col}\simeq a_0(L/L_d)=\hat{a}_{sp}^{dif}(L/L_d)$. A beam transition from collimated to optimally focused on the target surface results in an L/L_d-fold speckle-size increase. This example shows that during TIL system operation, the characteristic speckle size can vary over quite a wide range.

From the diffraction-limited speckle-size estimation $\hat{a}_{sp}^{dif}\simeq a_0$, it follows that diffraction-limited performance can be achieved in TIL wavefront control systems based on speckle-size metric optimization only if the receiver aperture size a_R is chosen to be significantly larger than the corresponding size of the transmitter aperture a_0. The condition $a_R>a_0$ is required in order to obtain a sufficient number of speckles inside the receiver aperture for speckle-size metric estimation in near-diffraction-limited TIL system operation.

4.6 Speckle-field intensity temporal fluctuations

Target surface and/or laser beam hit spot motion causes the speckle field inside the receiver aperture to change, resulting in temporal fluctuations of intensity at the observation point. To analyze these fluctuations, consider expression (4.17) for the speckle-field intensity MCF.

In expression (4.17), the influence of surface motion is associated with two terms that are dependent on the coordinate shift $\mathbf{v}_s\tau$: the product $A_T(\mathbf{r}')A_T^*(\mathbf{r}'+\mathbf{v}_s\tau)$, and the exponential term $\exp[ik\mathbf{r}'(\mathbf{v}_s\tau)/L]$. The term $A_T(\mathbf{r}')A_T^*(\mathbf{r}'+\mathbf{v}_s\tau)$ is nonzero only if the coordinate shift $|\mathbf{v}_s|\tau$ does not exceed the characteristic beam size b_s on the target surface. This condition defines the first characteristic time $\tau_s=b_s/v_s$ ($v_s=|\mathbf{v}_s|$) upon which the speckle-field intensity temporal correlation depends. The time τ_s corresponds to complete update of the surface roughness inside the target hit-spot area and defines the longest correlation time scale in the intensity fluctuation process. Temporal correlation is possible only when $\tau<\tau_s$.

Consider now the exponential term $\exp[ik\mathbf{r}'(\mathbf{v}_s\tau)/L]$ in Eq. (4.17). This term can be approximated by one when for all points $\mathbf{r}'$ inside the target hit-spot area of size b_s the condition $k\mathbf{r}'(\mathbf{v}_s\tau)/L\ll 1$ is fulfilled. This condition can be represented as $\tau\ll\tau_0$, where $\tau_0=L/(v_s kb_s)$ is the second characteristic time scale upon which the intensity fluctuation correlation properties depend. Using expression (4.23) for the speckle size, we obtain $\tau_0=L/(v_s kb_s)\simeq\hat{a}_{sp}/v_s$. The speckle-field intensity temporal correlation properties are dependent on the ratio of the two characteristic time scales τ_0/τ_s.

Assume first that $\tau_0/\tau_s\ll 1$ and $\tau\ll\tau_0$. In this case, the distance $v_s\tau$ is so small that in Eq. (4.17), we can use the approximation $A_T(\mathbf{r}'+\mathbf{v}_s\tau)\simeq A_T(\mathbf{r}')$. The spatiotemporal MCF $\Gamma_{\delta I}(\boldsymbol{\rho},\tau)$ can then be expressed through the spatial MCF, that is [48],

$$\Gamma_{\delta I}(\boldsymbol{\rho},\tau)=\Gamma_{\delta I}(\boldsymbol{\rho}-\mathbf{v}_s\tau). \tag{4.24}$$

Expression (4.24) shows that for the time scale $\tau\ll b_s/v_s$, all temporal changes in the speckle-field intensity at a fixed observation point only depend on the speckle-pattern motion as a whole. Note that the condition $\tau_0/\tau_s<1$ can be represented in the form $L<<kb_s^2$. This corresponds to the *near-field diffraction regime* for the TIL return beam in the absence of surface roughness.

In the near-field diffraction regime, speckles can move without change over distances that significantly exceed their size. In this case, the characteristic intensity temporal correlation time τ_c can be estimated as the time required for a speckle to cross the observation point $\tau_c=\hat{a}_{sp}/v_s=\tau_0$. Correspondingly, the intensity fluctuation temporal spectrum is localized within the frequency bandwidth

$$\omega_I\simeq 1/\tau_0=v_s kb_s/L. \tag{4.25}$$

Consider the opposite case where $\tau_0/\tau_s\gg 1$ and $\tau<\tau_s\ll\tau_0$. This condition corresponds to the *far-field (Fraunhofer) diffraction regime* ($L>kb_s^2$). In this regime, moving speckles change within distances that do not exceed the characteristic speckle size $\hat{a}_{sp}$. For $\tau<\tau_s\ll\tau_0$, the phase shift $k\mathbf{r}'(\mathbf{v}_s\tau)/L$ is small; hence, the exponential term $\exp[ik\mathbf{r}'(\mathbf{v}_s\tau)/L]$ can be substituted with one in Eq. (4.17).

The speckle-field intensity fluctuation MCF in the far-field diffraction regime is given by

$$\Gamma_{\delta I}(\boldsymbol{\rho},\tau)=\left(\frac{k}{2\pi L}\right)^4\left|\int A_T(\mathbf{r}')A_T^*(\mathbf{r}'+\mathbf{v}_s\tau)\exp[-ik\mathbf{r}'\boldsymbol{\rho}/L]\,d^2\mathbf{r}'\right|^2. \tag{4.26}$$

For the temporal correlation function in the far-field regime, we then obtain

$$\Gamma_{\delta I}(\tau)\equiv\Gamma_{\delta I}(\boldsymbol{\rho}=0,\tau)=\left(\frac{k}{2\pi L}\right)^4\left|\int A_T(\mathbf{r}')A_T^*(\mathbf{r}'+\mathbf{v}_s\tau)\,d^2\mathbf{r}'\right|^2. \tag{4.27}$$

From Eq. (4.27), for a Gaussian hit-spot intensity distribution at the target (4.22), we have

$$\Gamma_{\delta I}(\tau)=\Gamma_{\delta I}(0)\exp\left[-\frac{\tau^2}{2\tau_s^2}\right]=\Gamma_{\delta I}(0)\exp\left[-\frac{(v_s\tau)^2}{2b_s^2}\right]. \tag{4.28}$$

Correspondingly, the frequency spectrum $G_I(\omega)$ for the speckle-field intensity fluctuation at an observation point is determined by the Fourier transform of $\Gamma_{\delta I}(\tau)$ and is given by

$$G_I(\omega)=G_I(0)\exp\left[-\frac{\omega^2}{2(\omega_I)^2}\right], \tag{4.29}$$

where $\omega_I=v_s/b_s$ is the characteristic frequency bandwidth for intensity fluctuations at a point.

Note that the frequency spectrum bandwidth ω_I for speckle-field intensity fluctuations (in both the near- and far-field regimes) depends on the spatial extent (target hit-spot size) of the outgoing wave intensity distribution at the target surface [see Eqs. (4.25) and (4.29)]. This property is the basis for the TIL speckle metrics described below.

5 Aperture average intensity fluctuations and speckle metrics

5.1 Temporal correlation and power spectrum

In the previous analysis, the speckle-field intensity fluctuations were considered at a single point on the receiver plane (point measurements). In practice, return-field measurements are commonly performed using a receiver with finite aperture of size a_R. This corresponds to registration of the instantaneous value of the aperture-average speckle-field intensity, which is proportional to the power-in-the-bucket (PIB) signal (3.4)

$$J_{PIB}(t)=\int P(\mathbf{r})\,|\psi(\mathbf{r},z=0)|^2\,d^2\mathbf{r}=\int P(\mathbf{r})I_{sp}(\mathbf{r},t)\,d^2\mathbf{r}, \tag{5.1}$$

where $P(\mathbf{r})$ is the receiver telescope pupil function. In the case of a receiver telescope with circular aperture of radius a_R, the pupil function $P(\mathbf{r})=1$ for $|\mathbf{r}|\le a_R$, and $P(\mathbf{r})=0$ otherwise.

The time-varying component (fluctuation) of the PIB signal is defined as

$$\delta J_{PIB}(t)\equiv J_{PIB}(t)-\langle J_{PIB}(t)\rangle=\int P(\mathbf{r})\delta I_{sp}(\mathbf{r},t)\,d^2\mathbf{r}. \tag{5.2}$$

Note that the signal $\delta J_{PIB}(t)$ describing photocurrent fluctuations is proportional to the varying component of the PIB receiver sensor photocurrent.

Using Eq. (4.12), the temporal correlation function $\Gamma_{PIB}(\tau)$ of the PIB signal varying component can be represented in the form

$$\Gamma_{PIB}(\tau)\equiv\langle\delta J_{PIB}(t)\delta J_{PIB}(t+\tau)\rangle =\int P(\mathbf{r}_1)\,P(\mathbf{r}_2)\,\Gamma_{\delta I}(\mathbf{r}_1,\mathbf{r}_2,\tau)d^2\mathbf{r}_1d^2\mathbf{r}_2. \tag{5.3}$$

Assume that speckle-field propagation occurs either in an optically homogeneous medium, or in a medium with phase-distorting layers located only at either the receiver and/or target planes. In this case (see Subsection 4.4), the speckle-field intensity fluctuation mutual correlation function $\Gamma_{\delta I}(\mathbf{r}_1,\mathbf{r}_2,\tau)$ in Eq. (5.3) depends only on the difference coordinate $\boldsymbol{\rho}=\mathbf{r}_2-\mathbf{r}_1$. Correspondingly

$$\Gamma_{PIB}(\tau)=\int P(\mathbf{r}_1)\,P(\mathbf{r}_2)\,\Gamma_{\delta I}(\mathbf{r}_1,\mathbf{r}_2,\tau)d^2\mathbf{r}_1d^2\mathbf{r}_2 =\int M(\boldsymbol{\rho})\Gamma_{\delta I}(\boldsymbol{\rho},\tau)\,d^2\boldsymbol{\rho}, \tag{5.4}$$

where

$$M(\boldsymbol{\rho})=\int P(\mathbf{R}-\boldsymbol{\rho}/2)P(\mathbf{R}+\boldsymbol{\rho}/2)d^2\mathbf{R}. \tag{5.5}$$

Assume that the receiver aperture size a_R is significantly larger than the characteristic length of the function $\Gamma_{\delta I}(\rho,\tau)$ fall-off that defines the speckle size $\hat{a}_{sp}$. Within the area of size $\hat{a}_{sp}$ essential for integration over the variable $\boldsymbol{\rho}$ in Eq. (5.4), the function $M(\boldsymbol{\rho})$ can be approximated by a constant [$M(\boldsymbol{\rho})\approx M_0$].

Substitute expression (4.16) for the speckle-field intensity fluctuation MCF into Eq. (5.4). Assuming that $\Theta_a=0$, we obtain

$$\Gamma_{PIB}(\tau)=C\int\Gamma_{\delta I}(\boldsymbol{\rho},\tau)\,d^2\boldsymbol{\rho}=C\int\exp(ik\boldsymbol{\rho}'\boldsymbol{\rho}/L)d^2\boldsymbol{\rho}\times \int\exp(-ik\boldsymbol{\rho}'\mathbf{v}_s\tau/L)A_T(\mathbf{r}')A_T^*(\mathbf{r}'-\boldsymbol{\rho}') A_T^*(\mathbf{r}'+\mathbf{v}_s\tau)A_T(\mathbf{r}'+\mathbf{v}_s\tau-\boldsymbol{\rho}')d^2\mathbf{r}'d^2\boldsymbol{\rho}', \tag{5.6}$$

where $C=M_0[k/(2\pi L)]^4$. By taking into account that the integral over the variable $\boldsymbol{\rho}$ is proportional to the δ function $\delta(\boldsymbol{\rho}')$, Eq. (5.6) can be simplified [14, 48]:

$$\Gamma_{PIB}(\tau)=C\int I_T(\mathbf{r})I_T(\mathbf{r}+\mathbf{v}_s\tau)d^2\mathbf{r}, \tag{5.7}$$

where $I_T(\mathbf{r})\equiv I(\mathbf{r},L)$. Note that the correlation function $\Gamma_{PIB}(\tau)$ for the PIB signal-varying component (5.7) has the same form for both the near- and far-field diffraction regimes.

From a practical viewpoint, the use of the PIB signal fluctuation power spectrum $G_{PIB}(\omega)$ can be more convenient than the correlation function $\Gamma_{PIB}(\tau)$. In accordance with the Wiener-Khintchine theorem, $\Gamma_{PIB}(\tau)$ and $G_{PIB}(\omega)$ are linked by the Fourier transform relationship. [We assume that the varying component of the power-in-the-bucket signal (5.1) is a stationary random process.]

$$\begin{aligned} G_{PIB}(\omega)&=\frac{1}{\pi}\int_0^\infty \Gamma_{PIB}(\tau)\cos(\omega\tau)d\tau \\ &=\frac{C}{\pi}\int_0^\infty\int \cos(\omega\tau)I_T(\mathbf{r})I_T(\mathbf{r}+\mathbf{v}_s\tau)d^2\mathbf{r}d\tau, \end{aligned} \tag{5.8}$$

For a Gaussian-shaped intensity distribution $I_T(\mathbf{r})$ of size b_s, similar to Eq. (4.29), we obtain

$$G_{PIB}(\omega)=G_{PIB}(0)\exp\left[-\frac{\omega^2}{(\omega_{PIB})^2}\right], \tag{5.9}$$

where $\omega_{PIB}=v_s/b_s$ is the characteristic frequency bandwidth for PIB signal fluctuations. The PIB signal fluctuation power spectrum bandwidth increases with surface velocity and decreases with the target hit-spot size b_s. Note that for a Gaussian beam, the characteristic correlation time for PIB signal fluctuations $\tau_{PIB}=1/\omega_{PIB}$ coincides with the characteristic time of surface roughness realization update $\tau_{PIB}=\tau_s=b_s/v_s$.

5.2 Power-in-the-bucket fluctuation variance as a speckle metric

From expressions (5.7) and (5.8) follows an important property of power-in-the-bucket fluctuations – both the temporal correlation function $\Gamma_{PIB}(\tau)$ and power spectrum $G_{PIB}(\omega)$ of this signal depend on the target hit-spot intensity distribution $I_T(\mathbf{r})$. This property allows one to obtain a set of speckle metrics for wavefront phase control in TIL laser beam projection systems [14, 32, 50].

Consider first the variance σ^2_{PIB} for PIB signal fluctuations. The expression for σ^2_{PIB} can be obtained by substituting $\tau=0$ into Eq. (5.7)

$$\sigma^2_{PIB}=\Gamma_{PIB}(0)=<\delta J^2_{PIB}>=C\int I_T^2(\mathbf{r})d^2\mathbf{r}. \tag{5.10}$$

Using the Fourier transform relationship between $\Gamma_{PIB}(\tau)$ and $G_{PIB}(\omega)$, the PIB fluctuation variance can also be expressed through the temporal power spectrum $G_{PIB}(\omega)$ as

$$\sigma^2_{PIB}=\Gamma_{PIB}(0)=\int_0^\infty G_{PIB}(\omega)d\omega. \tag{5.11}$$

By comparing expressions (5.10) and (3.1), it follows that the PIB fluctuation variance is proportional to the target-plane metric sharpness function J_2, so that $\sigma^2_{PIB}=CJ_2$. This means that the variance σ^2_{PIB} can be considered as a speckle metric whose maximization results in an increase in the sharpness function [14].

Compare the efficiency of metrics $<J_{PIB}>$ and σ^2_{PIB}. As discussed in Subsection 3.3, the metric $<J_{PIB}>$ defined by Eq. (3.4) is proportional to the ensemble-average speckle-field intensity $<I_{sp}(\mathbf{r})>$ and can characterize the target hit-spot power density (hit-spot brightness) for relatively small (unresolved) targets or extended targets with a single bright glint. On the contrary, the metric σ^2_{PIB} is proportional to the target-plane beam quality metric J_2 and can only be applied for the target plane beam quality characterization for extended (resolved) targets. When the target size a_T becomes smaller so that $a_T<b_s$, the characteristic speckle size starts to be dependent on the target size, rather than on the beam size b_s, and correspondingly, the time-varying component δJ_{PIB} decreases. This results in the decrease in the signal-to-noise ratio measurements for σ^2_{PIB}. Note that for a point-source (unresolved) target, the variance σ^2_{PIB} is zero, and hence, it cannot be used as a performance metric.

These 'complimentary' properties of the time-average and time-varying components of the PIB signal can be used in the following combined speckle metric:

$$J^{\Sigma}_{PIB}\equiv\sigma^2_{PIB}+\beta<J_{PIB}>, \tag{5.12}$$

where $0<\beta\le 1$ is a weighting coefficient.

Speckle-metric (5.12) is useful in typical TIL laser beam projection scenarios, where the initial (prior to outgoing beam control) beam size b_s significantly exceeds the target size a_T (unresolved target), while the diffraction-limited (compensated) beam size b_s^{dif} is significantly smaller than a_T. Indeed, prior to compensation when $b_s>a_T$, the speckle- metric J^{Σ}_{PIB} only depends on the target-plane intensity distribution through the term $<J_{PIB}>$. The term σ^2_{PIB} in Eq. (5.12) is then determined only by the target size a_T and, hence, is independent of the target-plane beam size.

When b_s ($b_s\simeq a_T$) decreases, the metric component $<J_{PIB}>$ becomes less sensitive to the beam size, as

a major portion of the laser beam is already within the target surface area. On the contrary, the influence of the term σ^2_{PIB} increases. For $b_s<a_T$ (resolved target regime), the term $<J_{PIB}>$ is independent of the target hit-spot size, and dependence of the metric J^{Σ}_{PIB} on the target hit-spot size is only due to the term σ^2_{PIB}.

5.3 Speckle metrics based on received-signal temporal spectrum analysis

Consider some issues related with practical evaluation of the speckle-metrics $<J_{PIB}>$ and $\sigma^2_{PIB}=<\delta J^2_{PIB}>$. For a moving target surface, these metrics can be estimated by time averaging the measured power-in-the-bucket signal $J_{PIB}(t)$ (We assume that $J_{PIB}(t)$ is a stationary and ergotic random process.)

$$<J_{PIB}>\simeq\overline{J}_{PIB}=\frac{1}{T}\int_t^{t+T} J_{PIB}(\xi)d\xi, \tag{5.13}$$

$$\sigma^2_{PIB}\equiv<\delta J^2_{PIB}>\simeq\frac{1}{T}\int_t^{t+T}\left[J_{PIB}(\xi)-\overline{J}_{PIB}\right]^2 d\xi, \tag{5.14}$$

where T is the averaging (sampling) time. Note that $\overline{J}_{PIB}$ corresponds to the estimation of the mean value (dc component) of the signal $J_{PIB}(t)$ over the time interval $[t, t+T]$. In practice, the computation of $\overline{J}_{PIB}$ and σ^2_{PIB} in Eqs. (5.13) and (5.14) can be performed using either digital or analog signal multiplication and integration.

Another practical approach for speckle-metric evaluation is based on spectral analysis of sufficiently long sections of the signal $J_{PIB}(\xi)$ ($t\le\xi<t+T$). In this approach, registered sections of the signal $J_{PIB}(\xi)$ are first used for the computation of random spectrum realizations. These spectrum realizations are then averaged to obtain the power spectrum estimation $G^T_{PIB}(\omega)$.

In the spectral approach, the PIB metric $<J_{PIB}>$ corresponds to the zero spectral component of the power spectrum: $<J_{PIB}>\simeq G^T_{PIB}(\omega=0)$. The speckle-metric σ^2_{PIB} is determined by integrating the power spectrum $G^T_{PIB}(\omega)$ over the entire frequency band [see Eq. (5.11)].

An important advantage of the speckle-metrics (5.10) and (5.12) over the speckle-size metric (3.6) discussed in Section 3.5 is that the values $<J_{PIB}>$ and σ^2_{PIB} can be computed using measurements of the one-dimensional signal $J_{PIB}(t)$ obtained from a single photodetector, while speckle-size metric estimation requires processing of the two-dimensional speckle-intensity patterns $I_{sp}(\mathbf{r})$ (speckle images) registered by a high-resolution photo-array.

The primary disadvantage of the PIB speckle-metrics $<J_{PIB}>$ and σ^2_{PIB} is that their estimation requires the processing of sufficiently long sections of the signal $J_{PIB}(\xi)$: $t\le\xi<t+T$. This processing time is an important issue for TIL systems operated in the presence of dynamically changing (e.g., turbulence-induced) phase distortions, as the total time $\tau_J=T+\tau_{proc}$ required for speckle-metric estimation, including the sampling time T and the signal processing time τ_{proc} must be small in comparison with the characteristic time of phase distortion change: $\tau_J\ll\tau_{at}$. For simplicity, we assume that the signal processing time τ_{proc} is small in comparison with the sampling time and can be ignored, so that $\tau_J\simeq T$.

Consider the speckle-metric estimation error ε_T resulting from the PIB signal averaging over the finite sampling time T. This error depends on the shape of the PIB signal power spectrum $G_{PIB}(\omega)$ and the sampling time T [51]. For the error to be small requires that $T\gg 1/\omega_{PIB}$, where ω_{PIB} is the power spectrum bandwidth (cutoff) frequency. In this case, the error variance ε^2_T asymptotically approaches $G_{PIB}(\omega=0)/T$, indicating that a significant error contribution originates from the low-frequency spectral components [51].

Examples of typical power spectra $G^T_{PIB}(\omega)$ corresponding to different beam sizes on the moving target surface are shown in Figure 8. The power spectrum for the smaller beam (curve 1) is wider than the spectrum for the larger beam (curve 2). This dependence of the power spectrum on the target hit-spot size supports the physical basis for the described speckle metrics.

The use of the relatively short sampling time T causes large fluctuations in the low-frequency spectral components as clearly seen in Figure 8 where accuracy in determining spectral components is low. It follows that to decrease the error ε_T (without increasing the sampling time T) requires a decrease in the low-frequency contributions.

This goal can be achieved by increasing the power spectrum width (cutoff frequency ω_{PIB}) by fast steering of the outgoing laser beam. To estimate the requirements for steering speed, consider a beam with a Gaussian target-plane intensity distribution of size b_s. In accordance with Eq. (5.9), the power spectrum cutoff frequency is $\omega_{PIB}=v_s/b_s$.

Assume that for accurate speckle-metric estimation the required condition $1/\omega_{PIB}\ll T\ll\tau_{at}$ is satisfied if $1/\omega_{PIB}=b_s/v_s=10^{-2}T=10^{-4}\tau_{at}$. From this equality, we obtain $v_s\simeq(b_s/\tau_{at})\cdot 10^4$.

Consider as an example beam steering along a circuit of radius a_{st} that defines beam steering amplitude. In this case, for the steering frequency f_s (cycles/s), we obtain $f_s=1/T_s=v_s(2\pi a_{st})^{-1}=10^4 b_s/(2\pi a_{st}\tau_{at})$. For estimation, let

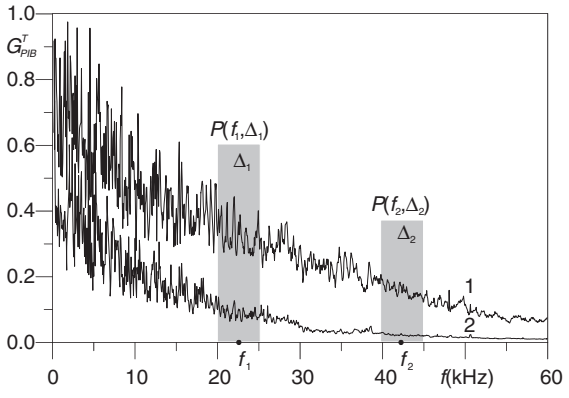

Figure 8 Normalized power-in-the-bucket fluctuation power spectra $G^T_{PIB}(f)$, ($f=\omega/2\pi$) experimentally obtained with the optical TIL system in Figure 5. The power spectra correspond to the target hit-spot size $b_s\approx0.2$ mm (1) and $b_s\approx0.6$ mm (2). The speckle field is produced by scattering the outgoing beam off the rough surface of a rotating metal disc. The linear speed in the vicinity of the target hit spot is $v_s\approx8$ m/s. The power spectrum $G^T_{PIB}(f)$ is computed by averaging a set of three random spectra calculated based on sequential sampling of the PIB signal $J_{PIB}(nT+m\Delta t)$ over time $T=13.5$ ms, where $n=0, 1, 2$, $m=0, \ldots, 2047$, and $\Delta t\approx6.6$ μs. Bars with central frequencies f_1 and f_2 and spectral widths Δ_1 and Δ_2 illustrate the band-pass filtering technique used for computation of the spectral metric (5.16). The values $P(f_1,\Delta_1)$ and $P(f_2,\Delta_2)$ correspond to the power spectrum integrated over the band-pass filter and are given by heights of the bars.

$\tau_{at}=5\cdot10^{-3}$ s, and $a_{st}=b_s$ (minimum distance that provides surface roughness update along the steering beam trajectory). It follows that $f_s\approx10$ MHz. This beam steering frequency can be achieved using coherent fiber-array beam projection systems with stair-mode wavefront dithering technique as described in Section 3.4 (see Figure 4) [33, 52].

The speckle-metric estimation error ε_T can be reduced using spectral filtering of the signal $J_{PIB}(t)$ prior to its processing. This implies that changes in the target hit-spot size can be estimated by integrating the power spectrum $G^T_{PIB}(\omega)$ only within one or several spectral regions (spectral bands) where the accuracy in determining the signal spectral components is high, as illustrated in Figure 8.

Consider the N selected power spectrum bands of widths Δ_j and central frequencies ω_j, ($j=1, \ldots, N$) and assume that the spectral components inside these spectral bands are integrated. This corresponds to the use of a bank of band-pass spectral filters. Output signal from the jth band-pass filter can be represented in the form

$$P(\omega_j,\Delta_j)=\int_{\omega_j-\Delta_j/2}^{\omega_j+\Delta_j/2} G_{PIB}(\omega)\,d\omega. \tag{5.15}$$

This band-pass filtering of the PIB fluctuation signal $J_{PIB}(t)$ gives rise to a spectral metric of the type [14, 46]

$$J_S=\sum_{j=1}^{N}\beta_j P(\omega_j,\Delta_j), \tag{5.16}$$

where β_j is the weighting coefficient. In contrast with the speckle-metric σ^2_{PIB} defined by Eq. (5.12), the power spectrum frequency components below $\omega_1-\Delta_1/2$ and higher than $\omega_N+\Delta_N/2$ do not contribute to the spectral metric J_S. Control of the parameters upon which spectral metric (5.16) depends (coefficients β_j, band-pass filter widths Δ_j, and central frequencies ω_j) allows optimization of the dependence of metric J_S on the target hit-spot intensity distribution.

In contrast with speckle metric σ^2_{PIB} whose value is directly associated with the target-plane metric J_2, a similar type of analytical expression linking metric J_S with a physically meaningful target-plane metric is not available. Nevertheless, both experiments and the following discussions support the arguments provided for the derivation of the metric (5.16) and demonstrate that with a correct selection of parameters in (5.16), the metric J_S can be used as a speckle metric, with its global maximum corresponding to the undistorted target hit-spot beam intensity distribution [14].

5.4 Experimental analysis of speckle metrics

The analytical expressions (4.19) and (5.4) upon which the speckle-field based metrics introduced above are based on are derived in Section 4 for somewhat idealized conditions: propagation in an optically homogeneous medium, near-normal incidence of the outgoing wave, small-angle scattering from a uniform metal surface with Gaussian roughness, etc. In practice, these conditions are not always satisfied. At the same time, such deviations from the idealized conditions as the propagation medium optical inhomogeneities, the non-Gaussian surface roughness, uneven target shape, etc., cannot be easily incorporated into the theory. On another hand, accurate computer simulation of TIL propagation, including scattering and speckle metric measurements that accounts for these factors represents quite a challenging problem. For this reason, experimental evaluation of the discussed speckle metrics plays an important role.

Such experimental analysis typically includes direct comparison of a selected speckle-metric J_{sp} with one or another target-plane metric J_T that characterizes the hit-spot intensity distribution, e.g., the beam size b_s on the target surface. The corresponding dependence $J_{sp}(J_T)$ is referred to as the *speckle-metric discrimination curve*. Note that in practice, it is more convenient to measure

dependence of speckle metrics not on target-plane metrics but on a controlling parameter upon which metric J_T monotonically depends on, such as the controlling voltage u_F applied to the deformable mirror electrode in Figure 6.

Consider the discrimination curves for the metrics $J_{sp}=\sigma^2_{PIB}$ and $J_{sp}=J_s$ shown in Figure 9. These discrimination curves were obtained in an experimental setup similar to the one shown in Figure 5 where a rotating metal disk with a size significantly exceeding the target hit-spot size was used as a moving target. The beam size b_s (the target-plane metric) on the target surface was varied by moving the target along the optical axis a distance Δz from the position (Δz=0) corresponding to the smallest beam size $b_s^{\min}$. Correspondingly, the target displacement Δz was used as a controlling parameter. Discrimination curves for the speckle metrics $J_{sp}=\sigma^2_{PIB}$ and $J_{sp}=J_s$ are shown on a logarithmic scale in Figure 9 [14].

Speckle-metric estimations were performed using analog processing of the power-in-the-bucket signal $J_{PIB}(t)$, which included PIB signal multiplication and time integration for the metric σ^2_{PIB}, and band-pass spectral filtering with output spectrum integration for the metric J_S.

All discrimination curves in Figure 9A have a maximum at the point of zero displacement (Δz=0) corresponding to the smallest possible beam size on the target. Note that for the metric J_s, the discrimination curve shape depends on the band-pass filter's central frequency f_1.

Similar analysis of the speckle-metric discrimination curves was performed for nonflat targets (metal sphere and cylinder), targets with various surface roughness correlation lengths l_s ranging from $l_s\simeq$10 μm to 300 μm, and tilted targets with a scattering angles between -20° and 20° [14]. In all cases examined, the metric discrimination curves had a single peak at Δz=0 corresponding to the smallest beam size on the target surface, although such characteristic discrimination shape parameters as peak value and width were different.

Consider as an example laser beam projection on a rapidly spinning aluminum cylinder (diameter b_T=10 mm) installed in a drill as shown in the inset photo in Figure 10A. In this experiment, the outgoing collimated laser beam of diameter D=25 mm was focused onto the target using a lens with focal distance F=200 cm. The projected beam size b_s varied by displacing the target from the lens focal plane. Figure 10A shows the measured dependencies $J_{sp}(b_s)$ for the following metrics: (a) spectral metric $J_{sp}=J_S=P(f_1,\Delta_1)$ with a single band-pass filter, where Δ_1=1.0 kHz and f_1=20 kHz; (b) the speckle-average power-in-the-bucket metric $J_{sp}=J_S=\langle J_{PIB}\rangle$; and (c) metric $J_{sp}=J_S+\langle J_{PIB}\rangle$, which is similar to the speckle metric (5.12).

The discrimination curves in Figure 10A illustrate the complimentary properties of metrics J_S and $\langle J_{PIB}\rangle$. The speckle-average PIB metric $\langle J_{PIB}\rangle$ is sensitive to the beam size at the target plane only when at least a portion of the beam energy misses the target. When a major portion of the laser beam is already within the target surface area, the metric $\langle J_{PIB}\rangle$ becomes less sensitive to the beam size. In the experiments described here, this occurs for the target hit-spot size $b_s<b_s^{PIB}\simeq 0.25 b_T$. This behavior of metric $\langle J_{PIB}\rangle$ suggests that optimization of this metric using an adaptive optics system can only partially decrease the target hit spot size.

On the contrary, spectral metric J_S is highly sensitive to the beam size only when the entire beam is located within the target surface area ($b_s<b_s^{PIB}$). Optimization of

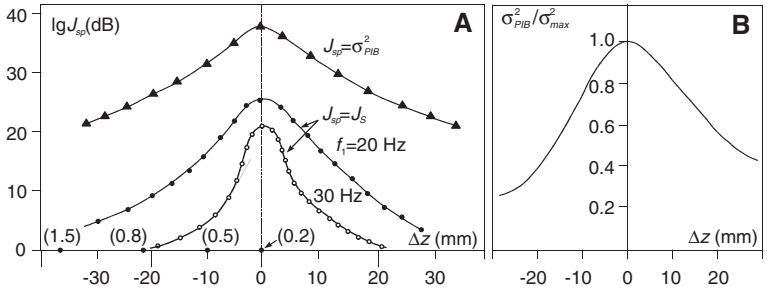

Figure 9 Dependence of the speckle metrics $J_{sp}=\sigma^2_{PIB}$ [Eq. (5.14)] and $J_{sp}=J_s$ [Eq. (5.16), N=1] on the target displacement Δz from the optimal position Δz=0 corresponding to the smallest beam size $b_s^{\min}$ at the target for laser beam projection on a rotating aluminum disc (A) and on a distorted water surface (B) used as the targets. Discrimination curves marked by circles correspond to a spectral metric with single band-pass filter $J_S=P(f_1,\Delta_1)$, where Δ_1=1.0 kHz, f_1=20 kHz for black circles, and f_1=30 kHz for white circles. Dots on the Δz axis and the corresponding numbers (in parentheses) correspond to the normalized target hit-spot size b_s. Surface roughness characteristics are correlation length $l_s\simeq$60 μm, roughness slopes $\theta_s=\sigma_s/l_s\simeq$1.0 rad (estimated based on the scattered wave angular divergence), and surface speed $v_s\simeq$8.0 m/s. For case (B), speckles resulted from the outgoing beam scattering of small amplitude water-surface waves excited by a piezo-vibrometer operating at 1.0 kHz frequency. The speckle metric $j_{sp}=\sigma^2_{PIB}$ in (B) is normalized by $\sigma^2_{max}=\max\sigma^2_{PIB}$.

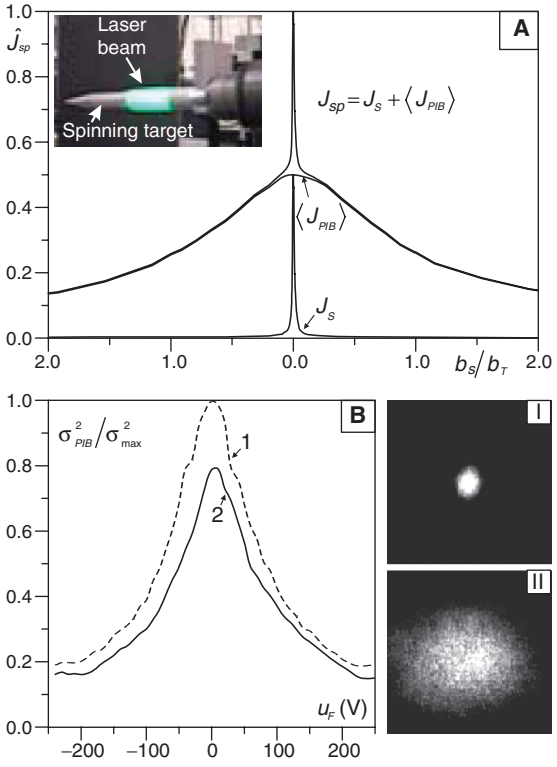

Figure 10 Speckle-metric discrimination curves measured in a beam projection experimental setup similar to the one in Figure 4. The targets are a spinning aluminum cylinder in (A) and rotating disk in (B). The spinning target with projected laser beam is shown in the photo insert in (A). Normalized speckle metrics J_S, $\langle J_{PIB}\rangle$, and $J_{sp}=\langle J_{PIB}\rangle+J_S$ are shown in (A) as functions of the normalized target hit-spot size b_s/b_T, where b_T is the cylinder diameter. Metrics σ^2_{PIB} in (B) are functions of the control voltage u_F applied to the deformable mirror. They correspond to propagation in an optically homogeneous (1) and turbulent (2) medium. Turbulence was created using two baseboard electrical heaters placed 1/3 and 2/3 of the distance between the transmitter telescope and target. The laser beam propagated through different sections of the heated air three times. This corresponds to the presence of six uncorrelated, equidistant phase-distorting layers located along L=70 m propagation distance. Gray-scale images (I) and (II) in (B) correspond to the laser beam hit spot on the rotating disc for optimal focusing conditions (u_F=0): (I) without turbulence and (II) with turbulence.

this metric using an adaptive optics system can potentially lead to a nearly diffraction-limited beam size at the target surface, but only if the target hit spot is reduced prior to optimization so that the speckle field characteristics are determined only by the size of the target-plane beam and are independent of the target size b_T.

From this viewpoint, the speckle metric $J_{sp}=J_S=\langle J_{PIB}\rangle$ has an obvious advantage as it can be used to reduce an initially (even highly) defocused beam of size $b_s \gg b_T$ to a nearly diffraction-limited hit spot.

Speckle-metric 'robustness' with respect to surface roughness statistical characteristics is illustrated in Figure 9B, where the metric σ^2_{PIB} was obtained using measurements of the target-return optical wave that originated from outgoing wave scattering off a distorted water surface. Although statistical properties of the distorted water surface are different from the Gaussian roughness model discussed in Section 3, the discrimination curve $\sigma^2_{PIB}(\Delta z)$ has a similar shape with a single maximum at zero displacement (Δz=0). Note that for all scenarios of laser beam projection on extended targets considered, the power-in-the-bucket mean value $\langle J_{PIB}\rangle$ was practically independent of the beam size b_s and, hence, cannot be used as a speckle metric.

Now consider speckle-metric discrimination curve measurements based on outgoing beam steering on a stationary target [45]. The experimental analysis shows that beam steering amplitude a_{st} alters the discrimination curve contract that is characterized by the factor η=(max J_{sp}-min J_{sp})/(max J_{sp}+min J_{sp}), where min J_{sp} corresponds to the speckle metric value obtained with a highly defocused beam. For small steering amplitudes ($a_{st}<0.3b_s$), the discrimination curve $\sigma^2_{PIB}(\Delta z)$ contrast is low ($\eta<0.2$), and noise in metric measurements is high (low signal-to-noise ratio). When the scanning amplitude is increased, the discrimination curve contrast monotonically increases reaching a value of $\eta\approx0.9$ at the scanning amplitude $a_{st}\approx 2b_s$. A further increase in a_{st} typically does not change the discrimination curve's contrast.

Experiments with laser beam projection onto an extended target (in a system similar to the one shown in Figure 4) with both outgoing and speckle-field propagation through a set of dynamically changing phase-distorting layers show that the presence of phase distortions along the propagation path does not change the most important speckle-metric property for TIL wavefront control applications – the monotonic dependence of these metrics on the target hit-spot size [14, 45].

As an example, Figure 10B illustrates dependence of the speckle-metric σ^2_{PIB} on the controlling voltage u_F applied to the deformable mirror (see Figure 4). The speckle metric σ^2_{PIB} was obtained for speckle-field propagation through a set of six equidistantly located phase-distorting layers (laboratory-generated turbulence). Use of a deformable mirror with controllable curvature made it possible to vary the beam size on the target. The system was aligned so that the smallest beam size corresponded to u_F=0. The speckle-metric discrimination curve measured in the presence of turbulence is compared in Figure 10B with the corresponding discrimination curve obtained without turbulence (curve 1). In both cases, the speckle-metric

discrimination curve maximum corresponds to the smallest beam footprint size on the target surface. The influence of dynamically changing optical inhomogeneities in the propagation medium on speckle-field propagation and speckle-metric characteristics are analyzed in [53].

6 Conclusion

Target-in-the-loop propagation in an optically inhomogeneous medium such as the atmosphere has attracted much attention with the increased use of optical systems operated with extended noncooperative targets such as laser tracking and interrogation systems, laser vibrometers, active and synthetic-aperture imaging systems, laser lidars, and high-power laser beam projection and beam relay systems. Most of these systems are equipped with fast-framing sensors capable of instantaneously measuring target-return speckle field characteristics. This can provide rapid estimation of speckle-field statistical properties for mitigation of speckle effects and adaptive compensation of turbulence-induced wavefront aberrations. These new developments require an understanding of the physics of optical wave propagation and laser beam scattering off randomly rough target surfaces, as well as knowledge of the speckle-field statistical properties that are relevant to target-in-the-loop systems. This paper introduces these topics using (where it is possible) physics-based insights, rather than rigorous mathematical derivations.

Acknowledgments: This work was supported, in part, by the U.S. Air Force Office of Scientific Research MURI Contract FA9550-12-1-0449 and by the Cooperative Agreement between the University of Dayton and the U.S. Army Research Laboratory, Contract W911NF-09-2-0040.

Received September 16, 2013; accepted October 28, 2013

References

[1] P. Artal, S. Marcos, R. Navarro and D. Williams, J. Opt. Soc. Am. A 12, 195–201 (1995).
[2] L. Diaz-Santana and J. C. Dainty, J. Opt. Soc. Am. A 18, 1437–1444 (2001).
[3] A. I. Saichev, Izv. Vyssh. Uchebn. Zaved. Radiofiz. 21, 1290–1293 (1978), [Radiophys. Quantum Electron. 21(9), 895–897 (1978)].
[4] Y. Kuga and A. Ishimaru, J. Opt. Soc. Am. A 1, 831–835 (1984).
[5] V. A. Banakh and V. L. Mironov, 'Lidar in a Turbulent Atmosphere' (Artech House, Dedham, Mass., 1987).
[6] Y. N. Barabanenkov, Y. A. Kravtsov, V. D. Ozrin and A. I. Saichev, in 'Progress in Optics', Ed. By E. Wolf (North-Holland, Amsterdam, 1991) Vol. 29, pp. 65–197.
[7] J. F. Holmes, Appl. Opt. 30, 2643–2646 (1991).
[8] Y. A. Kravtsov, Appl. Opt. 32, 2681–2691 (1993).
[9] L. C. Andrews, R. L. Phillips and C. Y. Hopen, Laser Beam Scintillation with Aplications, Vol. PM99 of Press Monograph Series (SPIE Press, Bellingham, Wash., 2001).
[10] M. A. Vorontsov and V. V. Kolosov, J. Opt. Soc. Am. A 22, 126–141 (2005).
[11] M. A. Vorontsov, V. V. Kolosov and A. Kohnle, J. Opt. Soc. Am. A 24, 1975–1993 (2007).
[12] M. A. Vorontsov, V. V. Kolosov and E. Polnau, Appl. Opt. 48, A13–A29 (2009).
[13] J. W. Hardy, 'Adaptive Optics for Astronomical Telescopes' (Oxford University Press, New York, 1998).
[14] M. A. Vorontsov and V. I. Shmal'hauzen, Principles of Adaptive Optics (Nauka, Moscow, 1985).
[15] M. A. Vorontsov and G. W. Carhart, Opt. Lett. 27, 2155–2157 (2002).
[16] L. I. Mandelstam, Ann. Phys. (Leipzig) 41, 609–624 (1913).
[17] F. G. Bass and I. M. Fuks, 'Wave Scattering from Statistically Rough Surfaces', Vol. 93 of International Series in Natural Philosophy (Pergamon Press, Oxford, 1979).
[18] A. Ishimaru, 'Wave Propagation and Scattering in Random Media' (Academic Press, New York, 1978).
[19] V. I. Tatarskii and W. V. Tatarskii, Wave. Random Media 4, 191–214 (1994).
[20] S. M. Rytov, Y. A. Kravtsov and V. I. Tatarskii, 'Principles of Statistical Radiophysics IV: Wave Propagation Through Random Media' (Springer-Verlag, Berlin, 1989).
[21] P. Beckmann and A. Spizzichino, 'The Scattering of Electromagnetic Waves from Rough Surfaces' (Pergamon Press, New York, 1963).
[22] A. V. Shchegrov, A. A. Maradudin and E. R. Mendez, in 'Progress in Optics', Ed. By E. Wolf (Elsevier, Amsterdam, 2004) Vol. 46, pp. 117–241.
[23] J. S. Chen and A. Ishimaru, J. Acoust. Soc. Am. 88, 1846–1850 (1990).
[24] E. R. Mendez and K. A. O'Donnell, Opt. Comm. 61, 91–95 (1987).
[25] A. R. McGurn, A. A. Maradudin and V. Celli, Phys. Rev. B 31, 4866–4871 (1985).
[26] V. V. Tamoikin and A. A. Fraiman, Izv. Vyssh. Uchebn. Zaved. Radiofiz. 11, 56–65 (1968), [Radiophys. Quantum Electron., 11(1), 31–36 (1968)].
[27] L. Mandel and E. Wolf, 'Optical Coherence and Quantum Optics' (Cambridge University Press, Cambridge, 1995).
[28] N. G. Denisov, Sov. Geomagnetizm and Aironomia 4, 675 (1964).
[29] J. C. Erdmann and R. I. Gellert, J. Opt. Soc. Am. 66, 1194–1204 (1976).

[30] M. A. Vorontsov, G. W. Carhart, D. V. Pruidze, J. C. Ricklin and D. G. Voelz, Appl. Opt. 36, 3319–3328 (1997).
[31] R. Dou, D. V. Pruidze, J. C. Ricklin, V. P. Sivokon and M. A. Vorontsov, in 'Propagation and Imaging Through the Atmosphere', Ed. By L. R. Bissonnette and C. Dainty, Proc. SPIE, 3125, 339–343 (1997).
[32] M. A. Vorontsov, V. N. Karnaukhov, A. L. Kuz'minskii and V. I. Shmal'gauzen, Kvant. Elektron. 11, 1128–1137 (1984), [*Sov. J. Quantum Electron.* 14 (6), 761–766 (1984)].
[33] M. Vorontsov, T. Weyrauch, S. Lachinova, M. Gatz and G. Carhart, Opt. Lett. 37, 2802–2804 (2012).
[34] M. T. Valley and M. A. Vorontsov eds, 'Target-in-the-Loop: Atmospheric Tracking, Imaging, and Compensation', Vol. 5552 of Proc. SPIE (SPIE, Bellingham, Wash., 2004).
[35] T. R. O'Meara, J. Opt. Soc. Am. 67, 306–315 (1977).
[36] N. C. Mehta and C. W. Allen, J. Opt. Soc. Am. A 11, 434–443 (1994).
[37] M. A. Vorontsov, G. W. Carhart, M. Cohen and G. Cauwenberghs, J. Opt. Soc. Am. A 17, 1440–1453 (2000).
[38] S. A. Kokorowski, M. E. Pedinoff and J. E. Pearson, J. Opt. Soc. Am. 67, 333–345 (1977).
[39] R. A. Muller and A. Buffington, J. Opt. Soc. Am. 64, 1200–1210 (1974).
[40] M. A. Vorontsov and S. L. Lachinova, J. Opt. Soc. Am. A 25, 1949–1959 (2008).
[41] M. A. Vorontsov, T. Weyrauch, L. A. Beresnev, G. W. Carhart, L. Liu, et al., IEEE J. Sel. Top. Quantum Electron. 15, 269–280 (2009).
[42] A. Brignon Ed., 'Coherent Laser Beam Combining' (Wiley-VCH, Weinheim, 2013).
[43] M. A. Vorontsov and V. P. Sivokon, J. Opt. Soc. Am. A 15, 2745–2758 (1998).
[44] T. Weyrauch and M. A. Vorontsov, Appl. Opt. 44, 6388–6401 (2005).
[45] V. I. Polejaev and M. A. Vorontsov, in 'Adaptive Optics and Applications', Ed. By R. Tyson and R. Fugate, Proc. SPIE, 3126, 216–220 (1997).
[46] M. A. Vorontsov, G. W. Carhart, D. V. Pruidze, J. C. Ricklin and D. G. Voelz, J. Opt. Soc. Am. A 13, 1456–1466 (1996).
[47] L. I. Goldfischer, J. Opt. Soc. Am. 55, 247–253 (1965).
[48] V. V. Anisimov, C. M. Kozel and G. R. Sov, Radio-physics and Electronics 15, 539 (1970).
[49] J. C. Dainty Ed., 'Laser Speckle and Related Phenomena', 2nd ed. (Springer-Verlag, Berlin, 1984).
[50] M. A. Vorontsov and V. I. Shmal'gauzen, Izv. Vyssh. Uchebn. Zaved. Radiofiz. 25, 1179–1187 (1982), [Radiophys. Quantum Electron. 25(10), 843–849 (1982)].
[51] S. A. Akhmanov, Y. E. D'yakov and A. S. Chirkin, 'Introduction to Statistical Radiophisics and Optics' (Nauka, Moscow, 1981).
[52] M. Vorontsov, T. Weyrauch, S. Lachinova, T. Ryan, A. Deck, et al., in 'Coherent Laser Beam Combining', Ed. By A. Brignon (Wiley-VCH, Weinheim, 2013) chap. 6, pp. 167–191.
[53] V. V. Dudorov, M. A. Vorontsov and V. V. Kolosov, J. Opt. Soc. Am. A 23, 1924–1936 (2006).

Mikhail A. Vorontsov received his PhD in Physics in 1977 and his Doctor of Science in Physics and Mathematics in 1989, both from the Lomonosov Moscow State University. Currently, he is a Professor and Wright Brothers Endowed Chair at the University of Dayton, research professor at the University of Maryland, College Park, and founder and CTO of Optonicus LLC. From 1997 to 2009, he was a senior physicist and Director of the Intelligent Optics Laboratory in the Computational and Information Sciences Directorate of the Army Research Laboratory. He has published over 300 papers and four books on the subjects of adaptive optics, atmospheric characterization, beam control, nonlinear spatiotemporal dynamics, and image processing. He is an SPIE and OSA Fellow.